Water treatment by cavitation: Understanding it at a single bubble - bacterial cell level

Žiga Pandur [a,b], Jure Zevnik [a], Darjan Podbevšek [a,c], Biljana Stojković [a], David Stopar [b,*], Matevž Dular [a,*]

[a] Faculty of Mechanical Engineering, University of Ljubljana, Askerceva 6, 1000 Ljubljana, Slovenia
[b] Biotechnical Faculty, University of Ljubljana, Jamnikarjeva 101, 1000 Ljubljana, Slovenia
[c] Advanced Science Research Center at The Graduate Center of the City University of New York, 85 Saint Nicholas Terrace, New York, USA

ARTICLE INFO

ABSTRACT

Cavitation is a potentially useful phenomenon accompanied by extreme conditions, which is one of the reasons for its increased use in a variety of applications, such as surface cleaning, enhanced chemistry, and water treatment. Yet, we are still not able to answer many fundamental questions related to efficacy and effectiveness of cavitation treatment, such as: "Can single bubbles destroy contaminants?" and "What precisely is the mechanism behind bubble's cleaning power?". For these reasons, the present paper addresses cavitation as a tool for eradication and removal of wall-bound bacteria at a fundamental level of a single microbubble and a bacterial cell. We present a method to study bubble-bacteria interaction on a nano- to microscale resolution in both space and time. The method allows for accurate and fast positioning of a single microbubble above the individual wall-bound bacterial cell with optical tweezers and triggering of a violent microscale cavitation event, which either results in mechanical removal or destruction of the bacterial cell. Results on *E. coli* bacteria show that only cells in the immediate vicinity of the microbubble are affected, and that a very high likelihood of cell detachment and cell death exists for cells located directly under the center of a bubble. Further details behind near-wall microbubble dynamics are revealed by numerical simulations, which demonstrate that a water jet resulting from a near-wall bubble implosion is the primary mechanism of wall-bound cell damage. The results suggest that peak hydrodynamic forces as high as 0.8 μN and 1.2 μN are required to achieve consistent *E. coli* bacterial cell detachment or death with high frequency mechanical perturbations on a nano- to microsecond time scale. Understanding of the cavitation phenomenon at a fundamental level of a single bubble will enable further optimization of novel water treatment and surface cleaning technologies to provide more efficient and chemical-free processes.

1. Introduction

Cavitation, rapid vaporization and bubble collapse due to a local change in pressure, is a widely used method in industry and research for cleaning, disinfection, dispersion, cell disruption, and isolation of cell components (Zupanc et al., 2019). Furthermore, it is recognized as effective and chemical free novel advanced water and wastewater treatment process (Šarc et al., 2016; Zupanc et al., 2019, 2014). The macroscopic effects of cavitation on bacteria are the results of implosions of a large number of bubbles (Gogate and Pandit, 2005; Paliwal and Mitragotri, 2006; Zupanc et al., 2019). However, the effects of the large bubble clusters do not reveal the inherent nature of cavitation and

a plethora of possible cavitation modes of action on bacteria (mechanical, physical, chemical). As stated by Prosperetti, thousands of papers have been devoted to the subject of bubbles, yet the exact mode of action of the bubble has not been elucidated (Prosperetti, 2004). To evaluate the effect of cavitation on bacteria at a fundamental level, one needs to downscale the cavitation process to a single cavitation bubble which is similar in size to a bacterial cell. To do so, spatio-temporal control of a single cavitation microbubble is required which is currently missing. In this work we test the effect of high frequency mechanical stress produced by a single microbubble on bacterial ability to survive. The cavitation microbubble forms when formation of micrometer sized vapor and gas cavities inside a liquid medium are followed by a violent
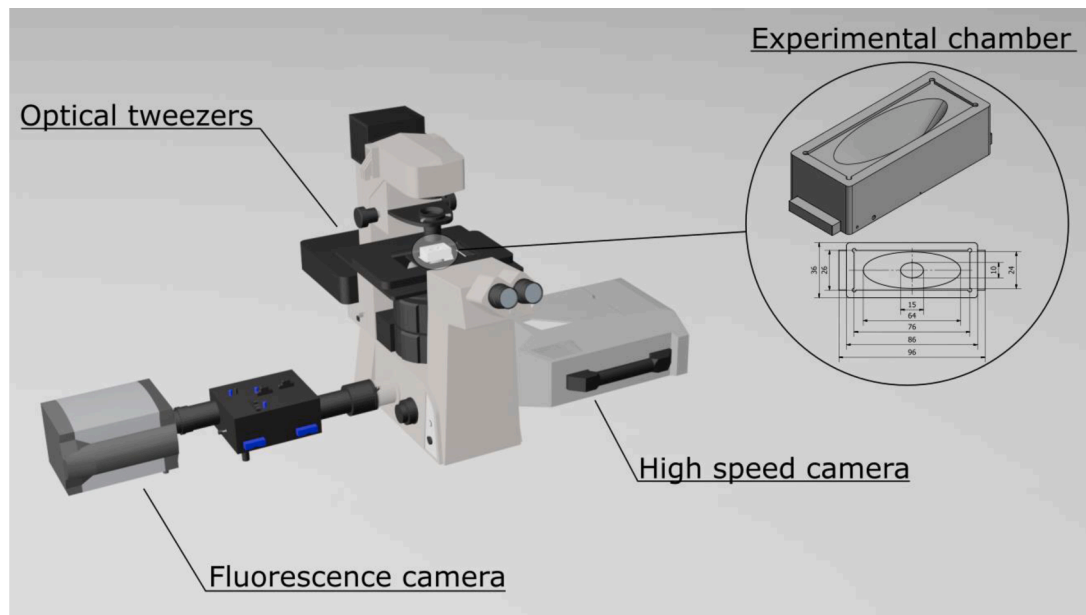

Fig. 1. Schematic diagram of the experimental setup. Optical tweezer system and pressure waves were used to trigger cavitation microbubble collapse. High speed and fluorescent cameras were used to observe the bubble evolution (and the response of the bacteria).

cavitation implosion on a nano- to microsecond time scale.

Time dependent response of bacteria to mechanical stress reveals a rubbery cell material response at low frequencies, viscoelastic response at intermediate frequencies, and glassy response at high frequencies (Vadillo-Rodríguez and Dutcher, 2011). The intermediate frequency regime corresponds to a characteristic time of cell growth when the cell is optimally adapted to the environment and most difficult to eradicate. From a material point of view, bacteria should be most susceptible to mechanical stress and consequently to destruction when exposed to high frequencies when cell wall material behavior changes from ductile to brittle and irreversible changes in cell wall structure are likely to occur. Whereas bacterial response to low and intermediate mechanical stress frequencies are well characterized by atomic force microscopy, laminar flow studies, and growth studies in confined spaces (Amir et al., 2014; Tuson et al., 2012; Vezenov and Barrett, 2013), the bacterial response to high frequency mechanical stress (i.e., in the micro- or nanosecond domain) is not well documented.

The interactions of a cavitation bubble, tens of micrometers in size, with eukaryotic cells have been described (Jasikova et al., 2019; O'Connor et al., 2021; Ohl et al., 2006; Rau et al., 2006). Mostly laser induced cavitation was used to provide controllable bubble collapse. However, due to intense laser irradiance, plasma formation, and reactive species development (Patinglag et al., 2021; Sinibaldi et al., 2019), the mechanical effects of cavitation on eukaryotic cells may be largely masked. In contrast to eukaryotic cells, single bubble – bacteria interactions have not been studied. Mainly due to unreliable production of micrometer size cavitation bubbles, lack of the ability to manipulate and position bubbles at a desired location, and small size of bacteria and microbubbles which are close to the diffraction limit of the light microscope.

We show the development of a new method, which enables a real time evaluation of the bacterial response to the mechanical stress induced by a single microbubble cavitation event on a nano- to microsecond time scale. The combination of optical tweezers and pressure waves enabled an accurate and fast positioning of a single microbubble and controlled induction of single microbubble cavitation event. With the optical tweezer we have produced a stable single nucleation bubble in the vicinity of the bacterial cell. The microbubble cavitation was triggered remotely with high voltage electric discharge which promoted pressure waves through the medium and induced nucleation

microbubble growth and collapse observed with high-speed camera. Direct observation of the interaction between a single cavitation microbubble and the individual bacterial cell is presented. The evolution of the fluid flow field during the microbubble collapse was characterized by silica bead displacements, which enabled in situ measurement of the fluid velocity field during the single cavitation event. The effect of a single microbubble on bacterial cell viability was recorded by fluorescence microscopy. The experimental results were used to validate the results of the numerical model, where the evolution of the single microbubble cavitation and its interaction with a bacterial cell was simulated. The threshold wall shear stress and hydrodynamic force needed for cell detachment and bacterial death during the single microbubble cavitation event were estimated.

2. Methods

2.1. Single microbubble generation

To generate micrometer sized cavities a combination of optical tweezers and high voltage electric discharge was used. Laser focusing was applied to generate a stable micrometer sized vapor microbubble which served as an initial microbubble nucleus. Then tension wave from spark discharge was used to promote nucleus expansion and consequent violent collapse – all on a micrometer size. Both systems were combined in a small 3D printed chamber.

Microbubble chamber design

Custom made conical elliptically shaped chamber was 3D printed. The technical drawing of the experimental chamber design is shown in Fig. 1. The bigger oval opening was covered with microscopic glass slide (76×26 mm, Menzel Gläser, Germany) and sealed with epoxy adhesive. Smaller oval opening was covered with #1.5 cover glass (60×24 mm, Menzel Gläser, Germany) and sealed with VALAP sealant mixture (mixture of Vaseline, lanoline, paraffin) ("Valap Sealant," 2015). For spark discharge, tungsten needles were placed in the center of the small oval opening approximately 0.5 mm above the cover glass. Chamber was filled with fresh deionized water (dH$_2$O, approx. 15 ml) with the addition of magnetic beads (final concentration approx. 3.7×10^6 beads/ml, Bangs Laboratories, USA). The assembled and filled experimental chamber was mounted on inverted microscope Nikon Eclipse Ti-U.
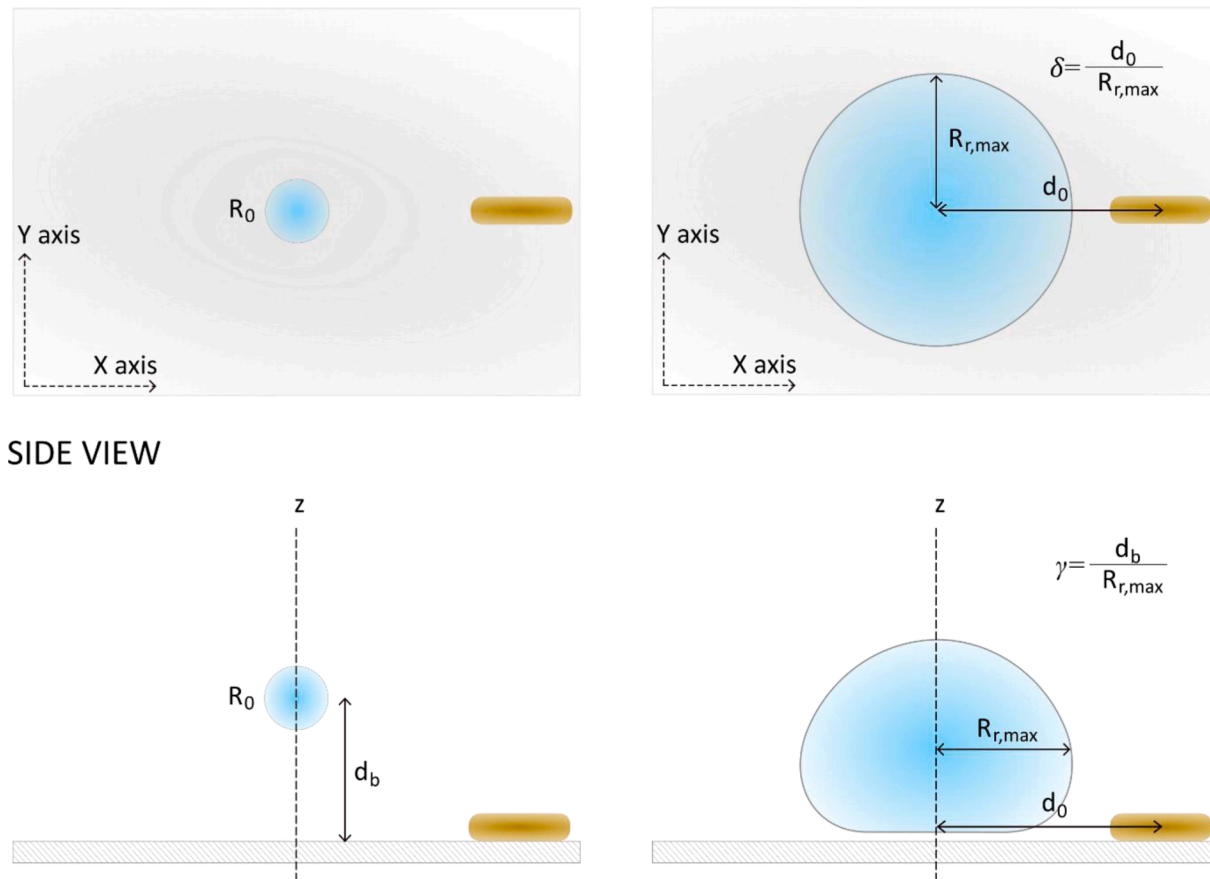
Fig. 2. A schematic representation of the microbubble-bacterium interaction at different perspectives: top view and side view. From the top view, d_0 represents the initial horizontal distance between the microbubble center and the bacterium proximal center where $R_{r,max}$ is the maximum microbubble radius. The non-dimensional distance δ represents the axial (horizontal) component of the microbubble-bacterium distance. From side view perspective, bottom left scheme shows a microbubble with initial radius R_0 and internal pressure p_0 is placed d_b away from the wall. Ambient liquid pressure and temperature are p_∞ and T_∞. Right image shows microbubble growth with maximum radius $R_{r,max}$.

Table 1
Material parameters used to model both phases, liquid – water and gas – air.

Material property [Unit]	Liquid phase - water	Gas phase - air
Dynamic viscosity μ [Pa s]	1.003×10^{-3}	1.8×10^{-5}
Thermal conductivity k [W/(m K)]	0.6	0.0242
Surface tension σ [N/m]	–	0.0728
Reference density ρ_{ref} [kg/m³]	998.2	–
Reference pressure p_{ref} [Pa]	101,325	–
Reference bulk modulus K_{ref} [Pa]	2.2×10^9	–
Density exponent n [-]	7.15	–
Specific gas constant R_g* [J/(kg K)]	–	287.05

Spark discharge bubble generation

During spark discharge, a millimeter size bubble was generated which upon spark discharge produced pressure waves (Fig. A1a). A piezoelectric actuator was used to produce a 16 kV pulsed spark discharge in the low conductive distilled water. A spring-loaded mechanical design ensures a repeatable strike on the piezoelectric ceramic actuator. The capacitance of the piezo actuator was estimated at roughly 30 pF. To accurately position electrical discharge in the medium, the micron sized tip of Tungsten surgical needles (Roboz surgical instrument RS-6065, 0.5 mm diameter, tapered to micrometer sized tip) were carefully placed at desired stand-off distances from each other. Mechanical driven piezo igniter unit was triggered via custom LabView script. With manipulation of the stand-off distances between the needles, the maximum spark discharge bubble radius could be varied (Fig. A1a). In a typical cavitation microbubble experiment the stand-off distance between the needles was 75 μm.

The stable nucleation microbubble generation

The stable nucleation microbubble was generated by the optical tweezer laser system (Aresis Tweez 300). The optical tweezer is equipped with 1064 nm wavelength laser (nominal power 5 W). Acousto-optic laser beam deflection system enables manipulation of micrometer sized particles on sub-micrometer resolution. Microparticles (i.e., gold and magnetite particles) have high absorption index in the near-infrared spectrum (Bhuyan et al., 2018; Quinto-Su, 2014). Irradiation of the microparticles with the laser beam causes heat transfer from the material to local medium which leads to vapor microbubble formation. A small micrometer sized nucleus on magnetic microbeads (Bangs Laboratories ProMag 3 Series - 3 μm particle diameter) was generated via local heating with high intensity laser pulse (laser irradiance approx. 2 $\times 10^8$ W/cm²). The optical tweezer was controlled by Tweez software (Aresis Ltd.). The laser was focused on the selected magnetic bead and laser pulse was released to generate the nucleus. Laser pulse duration was 17 μs at the maximum laser intensity. The positioning of magnetic beads at a desired location was done at low laser intensities (approx. 1000x reduced laser power compared to pulse used to generate nucleus). The nucleation microbubble lifetime was in millisecond to second range. When nucleus microbubble was coupled with shock waves generated by spark discharge bubble, the nucleus microbubble underwent violent growth and implosion on a microsecond time scale (Fig. 3a and Fig. A2).

High speed image recording

For visualization of microbubble collapse, microscope was coupled
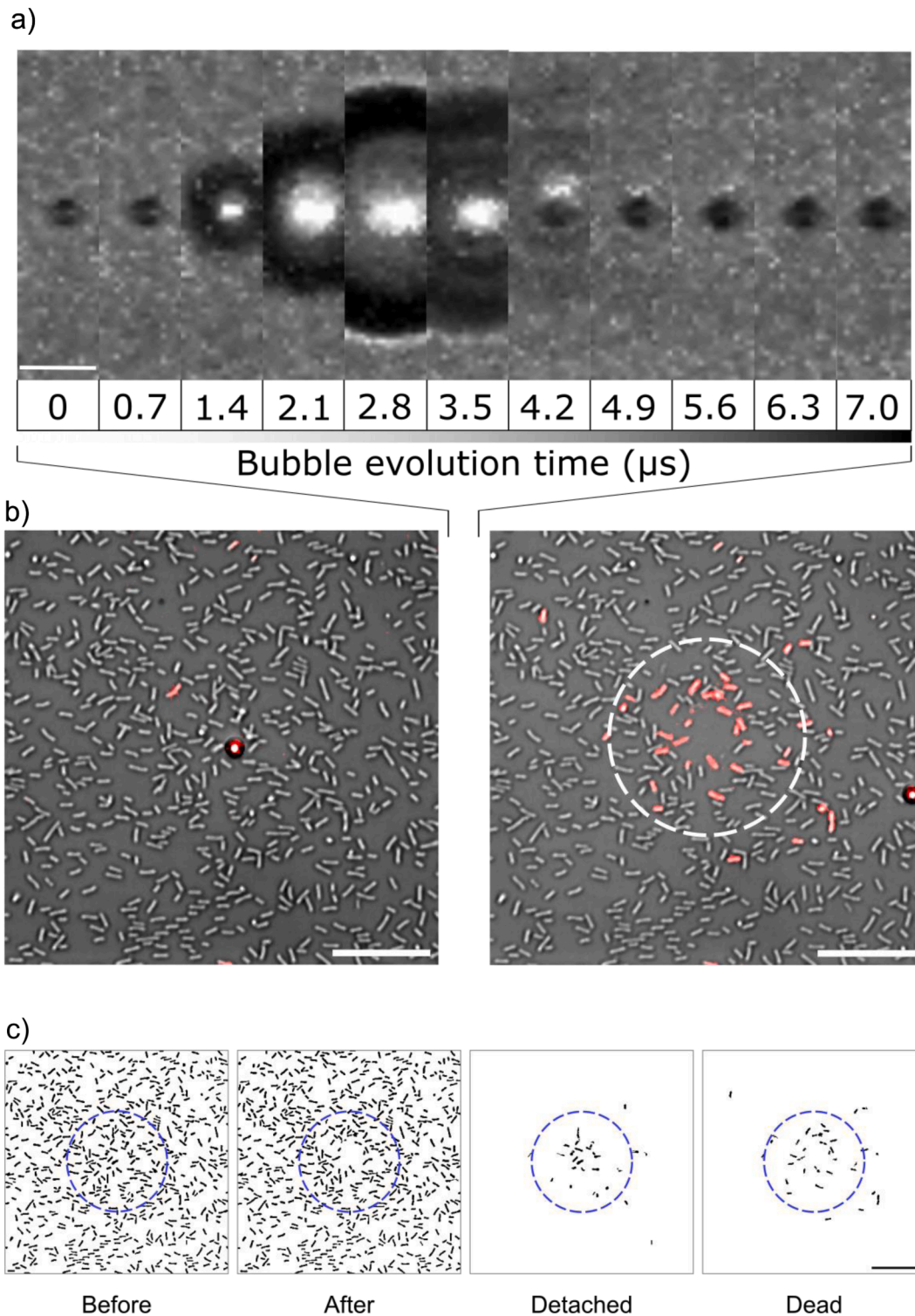
Fig. 3. Typical evolution of a cavitation microbubble and the recorded bacterial cell response. (**a**) High speed recorded images of microbubble collapse from the bottom view perspective. After propagation of compressive shock waves, a nucleation microbubble initially undergoes a phase of contraction. This is followed by focusing of a tensile wave, which leads to explosive microbubble expansion (1.4 – 2.8 μs) and then a microbubble collapse (3.5 μs and 4.2 μs). At the microbubble collapse phase (3.5 μs and 4.2 μs), the formation of a characteristic microjet (inner dark annulus – ring shaped structure within the bubble) towards the rigid surface may be observed. The sequence is 7 μs long, scale bar denotes 5 μm. (**b**) Microscopic images of attached bacterial cells (monolayer) before (left) and after (right) the microbubble collapse. Images are composite images from brightfield (gray) and fluorescence (red) channel. Red fluorescence channel represents cells stained with membrane impermeable PI dye (dead cells). Autofluorescence of magnetic bead is visible on the red channel. After microbubble collapse, most bacterial cells in proximity of the microbubble collapse are stained with PI (red) or were detached from the glass. A white dashed circle in the right image notes the projected maximal cavitation microbubble size. Scale bar marks 20 μm. (**c**) Binarized microscopic images presenting individual bacterial cells before and after the cavitation microbubble collapse event. Subtracting the images before and after the event reveals detached cells, whereas multiplication of fluorescence and brightfield microscope binary images yields dead cells. Blue dashed circle denotes the projected maximum cavitation microbubble radius $R_{r,max}$. Scale bar corresponds to 20 μm. (For interpretation of the references to colour in this figure legend, the reader is referred to the web version of this article.)
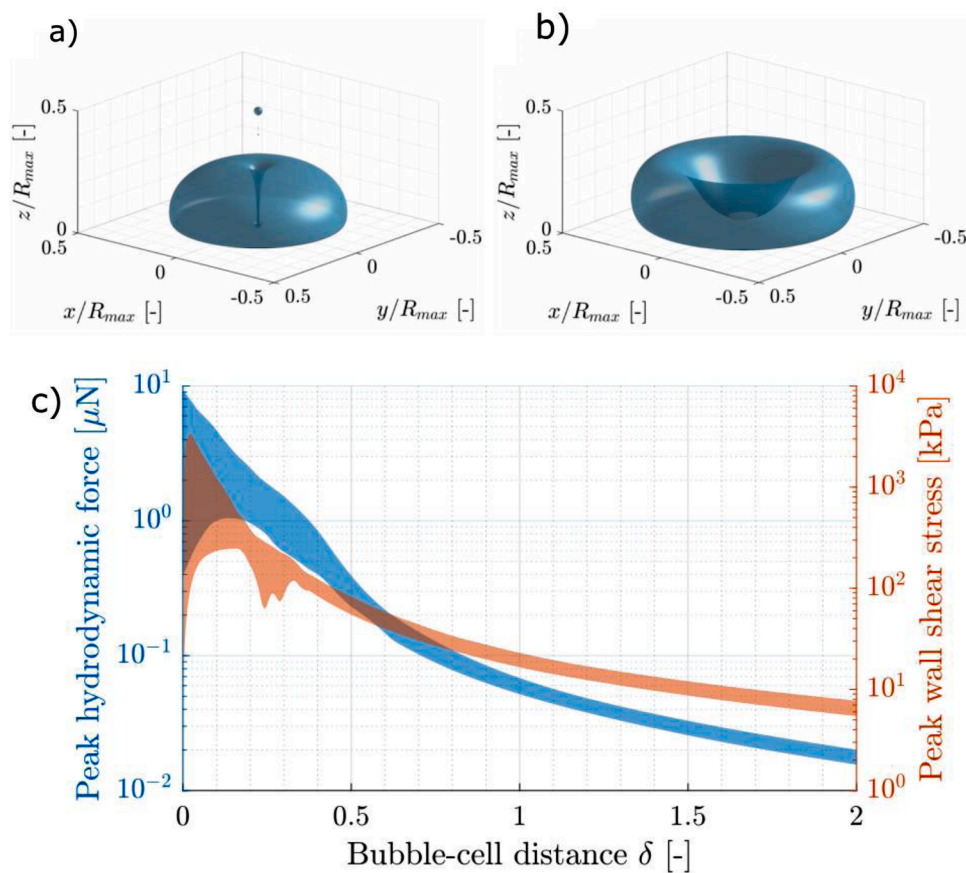
Fig. 4. Numerical results of near-wall microbubble dynamics and the resulting peak loads on nearby bacterial cells. (**a,b**) Numerical microbubble shape during the jet impact into the wall ($z = 0$) is given for both microbubble jetting mechanisms: (**a**) fast thin jet formation (γ=0.27) and (**b**) classical jet formation (γ=0.59). (**c**) Calculated peak hydrodynamics loads on nearby wall-bound bacterial cells in the form of hydrodynamic force (blue, left ordinate) and wall shear stress (orange, right ordinate). Both load metrics are given in relation to the non-dimensional microbubble-cell distance δ. Shaded area denotes the min-max envelope (blue and orange fill) obtained from numerical simulations for cases with γ between 0.15 and 0.58. A logarithmic scale is employed on both ordinates. (For interpretation of the references to colour in this figure legend, the reader is referred to the web version of this article.)

with high-speed recording camera Photron SA-Z type 2100K-M-64GB. For image acquisition of spark discharge bubble collapse, 10x magnification objective (Nikon CFI E Plan Achromat 10X) was used, with camera settings: frame rate 210,000 fps, 1 μs shutter speed, 384×160 px image resolution. For image acquisition of cavitation microbubble collapse, 60x magnification water immersion objective (Nikon CFI Apo NIR 60X W) was used and image sequences were taken at 1,440,000 fps, shutter speed 0.38 μs, and image resolution 128×16 px. Camera acquisition was synchronized with microbubble collapse by external trigger.

2.2. Bacteria

Growth and preparation of bacteria

Bacterial strain *Escherichia coli* MG1655 with green fluorescent protein (gfp) under IPTG inducible promotor expression was used. Frozen stock culture from −80 °C was plated on lysogeny broth (LB) agar plates with kanamycin-Kn (50 μg/ml). Single bacterial colony from LB plates was used as inoculum for an overnight bacterial culture in LB medium with kanamycin (50 μg/ml) and IPTG (400 μg/ml). Overnight medium was incubated at 37 °C, 200 rpm, in glass flasks under aerobic conditions for approximately 16 h.
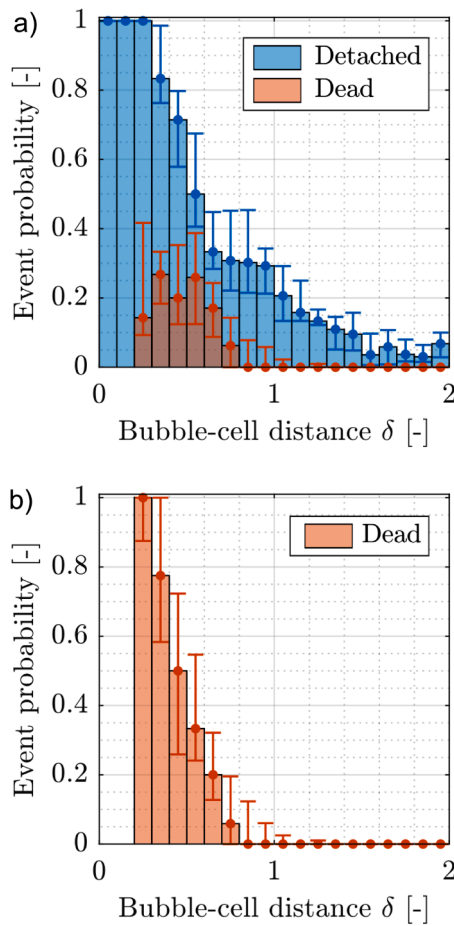
Bacterial attachment

#1.5 microscope cover glass dimensions 60×24 mm (Menzel-Gläser) was used for cell attachment. First, the glass was cleaned with sonication in 96% ethanol in ultrasonic bath (ASonic PRO MED 50, at 120 W, 40 kHz) for 20 min. After sonication, glass was rinsed with dH₂O and dried with compressed air. Additionally, glass was cleaned with plasma cleaner (Harrick Plasma) with air, at high radiofrequency power setting for 60 s. Right after the plasma cleaning, 50 μl of poly-L-Lysine (PLL) solution 0.1% (w/v) in water solution (Sigma-Aldrich, USA) was

dropped on the glass and incubated for 10 min at the room temperature. After the incubation, the cover glasses were rinsed with dH₂O and left to dry on air. The cover glasses were stored in dry and dark place until experiments. Next, 10 ml of the overnight bacterial culture was washed 3-times in dH₂O at 5000 rcf for 4 min. After the third supernatant removal, the bacterial pellet was resuspended in 100 μl of fresh dH₂O. To the cover glass covered with PLL, 50 μl of the concentrated bacterial culture was added and incubated for 5 min at room temperature to obtain homogenously distributed monolayer of single cells on glass surface. After incubation, unadhered cells were rinsed with dH₂O in a series of water baths. The cover glass was placed to the experimental chamber and sealed with VALAP. The experimental chamber was filled with dH₂O and magnetic beads as described above with the addition of 15 μl membrane impermeable dye (400 μM propidium iodide, PI) for fluorescence imaging of dead cells. Microbubble collapse was performed as described above.

Fluorescence microscopy

For visualization of bacteria, EMCCD camera (Andor Ixon 888 Ultra) equipped with Cairn Optosplit III image splitter system for multiple emission wavelengths spectrum was used. As excitation light source for fluorescence microscopy, CoolLed pE-4000 system was used. For visualization of viable bacterial cells with inducible gfp, sample was illuminated at 460 nm (30% intensity) and data recorded with emission filter 525/40 nm. For dead bacterial cells stained with PI dye, samples were illuminated with 550 nm wavelength (30% intensity) and emission filter 640/40 nm. Exposure time for both channels was 100 ms, acquisition interval of 5 s was used. Image size was: 1024×512 px (223.5 × 111.7 μm field of view). As fast fluorescence bleaching of gfp protein was observed, additional brightfield images were taken prior and after fluorescence imaging.

Fig. 5. Probability of the identified bacterial cell outcomes during a microbubble event. (**a**) Cell detachment (blue) and cell death (orange) probability of initial bacterial population in relation to the microbubble-cell distance parameter δ. (**b**) Cell death probability of non-detached cells (cells, attached after microbubble collapse, see Section 2.2, Data analysis). Experimental data is taken from 15 repeats ($11.1 \leq R_{r,max} \leq 24.4$ μm, median $R_{r,max}$=15.4 μm, $0.15 \leq \gamma \leq 0.58$, median γ=0.25), which yields a sample size of $N = 294$ for cell detachment and $N = 257$ for cell death. Both samples were obtained from 8646 cells in total. Data are binned into 20 equally spaced bins for δ between 0 and 2. Shown are median, 1st, and 3rd quartile of the cell event probability. In both plots (a, b), cell death probability for δ<0.2 is not given as all cells were detached. (For interpretation of the references to colour in this figure legend, the reader is referred to the web version of this article.)

Image analysis

Microscopic image analysis was performed with ImageJ (1.53f51) software. First, images from different acquired channels (brightfield, red and green fluorescence) were aligned in-between channels. Next, image analysis was performed through custom written ImageJ macro script to acquire positions of bacterial cells on the microscopic images. Center and maximum radius of microbubble were determined with high-speed camera and Photron Viewer PFV 4 software. Location of the microbubble center was determined on microscopic images. Images were trimmed to 2x of maximum microbubble radius. With the thresholded and trimmed brightfield images we obtained binary images of bacterial cells before and after microbubble collapse. The possible nearby magnetic beads were eliminated from the image analysis with subtracting area of the beads from binary images. To fully separate overlapping cells, additional manual review and segmentation of the cells was performed. On binary images, the location of each bacterium was determined before and after the cavitation microbubble collapse (plugin "Analyze Particles", with "Center of mass" measurement for location of bacterial cell on image. The detached cells were determined by

subtracting binary images before and after collapse. Additionally, we analyzed images from red fluorescence channel (PI dye) prior and after the cavitation microbubble collapse to determine the number of dead bacterial cells.

Data analysis

A schematic representation of the microbubble-bacterium interaction model at different perspectives is given in Fig. 2.

The cell locations obtained from image analysis were transformed into a non-dimensional distance δ as follows

$$\delta = \frac{\sqrt{\left(x_{cell} - x_{bubble\ center}\right)^2 + \left(y_{cell} - y_{bubble\ center}\right)^2}}{R_{r,max}}. \tag{1}$$

Here x and y denote the horizontal and vertical coordinate. A subscript "cell" denotes the corresponding coordinate of the cell center, whereas $R_{r,max}$ stands for the maximal projected bubble radius. Presently δ ranges between 0 (at the microbubble center) and 2 (two maximal radii away from the microbubble center). Each class of bacteria (initial state, detached cells, attached but dead cells, final state) was discretized into bins with width of $\Delta\delta = 0.1$ (20 bins in total). The probability of bacterial detachment and cell death for each experimental repeat was determined in relation to δ. The event probability for cell detachment and cell damage in the j-th bin of the i th experimental repeat was defined as follows

$$p_{detach}^{i,j} = \max\left[\frac{N_{detach}^{i,j}}{N_{cell,\ ini}^{i,j}}, \frac{N_{cell,ini}^{i,j} - N_{cell,final}^{i,j}}{N_{cell,ini}^{i,j}}\right], \tag{2}$$

$$p_{dead}^{i,j} = \frac{N_{dead}^{i,j}}{N_{cell,\ ini}^{i,j}}, \tag{3}$$

$$p_{dead,\ non\ detached}^{i,j} = \frac{N_{dead}^{i,j}}{N_{cell,\ final}^{i,j}}, \tag{4}$$

where $N_{cell,\ ini}^{i,j}$, $N_{cell,final}^{i,j}$, $N_{detach}^{i,j}$, and $N_{dead}^{i,j}$ denote the number of cells in the j-th bin of the i th experimental repeat at the initial and final state, the number of cells identified as detached and the number of dead cells, respectively. Cell death probability is determined in relation to both, the initial state and to the final state. The latter represents the cell death probability for non-detached cells only.

2.3. Numerical methods

Numerical simulations of near-wall microbubble dynamics were employed to reveal further details regarding bubble shape evolution and the resulting flow field. These results were then used to determine the hydrodynamic forces on nearby wall-bound bacterial cells according to the attached cell model. Validation of the employed methodology can be found in Appendix B and C.

Bubble dynamics model

The presently utilized bubble dynamics model (ANSYS®, 2021) is based on the finite volume method along with the volume of fluid method to resolve compressible multiphase flow. Two fluid phases are considered - a gas bubble and ambient liquid, and their interfaces are captured by solving continuity equations for the volume fraction field α_l of the liquid phase. Equation of mass conservation for the liquid phase can be written as

$$\frac{\partial \alpha_l \rho_l}{\partial t} + \nabla \cdot (\alpha_l \rho_l \boldsymbol{U}_l) = 0. \tag{5}$$

Here, ρ_l and $\boldsymbol{U}_l$ denote the density and velocity vector field of the liquid phase. The volume fraction field of the gas phase α_g can be obtained as $\alpha_g = 1 - \alpha_l$. After both volume fraction fields are known, we
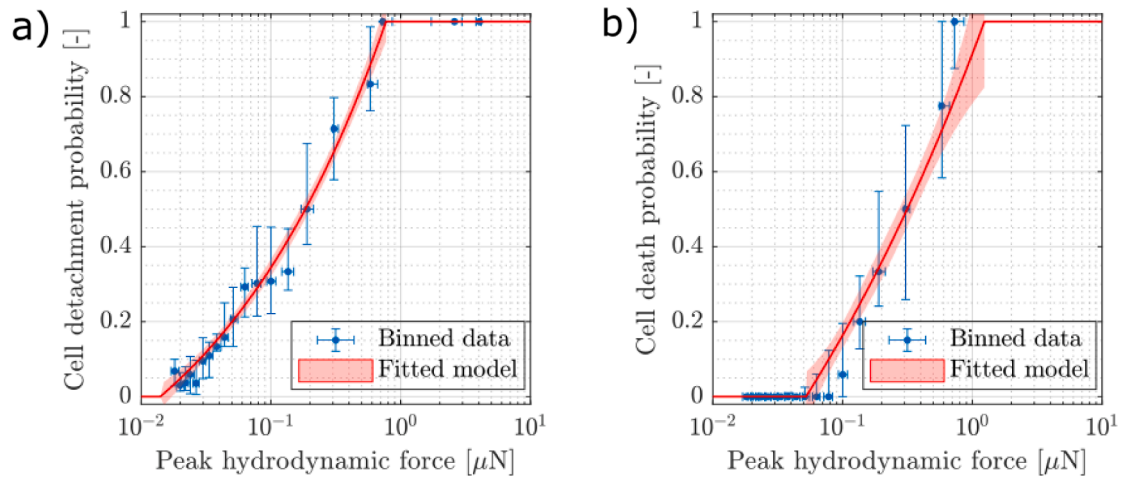
Fig. 6. Threshold mechanical loads for bacterial cell detachment and death during a single cavitation microbubble event. Fitted data (piecewise power law model) of experimental results (Fig. 5) and numerical results (Fig. 4c), which can be understood as threshold mechanical loads for bacterial cell death or detachment. Bacterial cell detachment (**a**) and death (**b**) probabilities plotted against peak hydrodynamic forces. Red line indicates the best fit of the cell event model along with 95% confidence intervals (red fill). Peak force results in the following goodness of fit metrics: cell detachment: R^2=0.89 and RMSE=0.11, cell death: R^2=0.68 and RMSE=0.15. Logarithmic scale is presented on abscissas. (For interpretation of the references to colour in this figure legend, the reader is referred to the web version of this article.)

Table 2

Determined threshold mechanical loads for E. coli detachment and death during a single cavitation microbubble event. P denotes the probability of a certain cell outcome.

Cell outcome	Mechanical load	Lower threshold $P \approx 0$	Upper threshold $P \approx 1$
Detachment	Force	14 ± 4 nN	0.8 ± 0.1 μN
	Wall shear stress	5.0 ± 1.5 kPa	145 ± 15 kPa
Death	Force	52 ± 14 nN	1.2 ± 0.5 μN
	Wall shear stress	18 ± 4 kPa	217 ± 61 kPa

can determine the volume-averaged fluid properties ϕ throughout the whole computational domain as $\phi = \sum_i \alpha_i \phi_i$. In the present case this is true for density ρ, dynamic viscosity μ, and thermal conductivity k. Based on the determined material properties, a single momentum (Eq. (6)) and energy (Eq. (7)) equation can be solved, which yields the shared velocity U and temperature T fields.

$$\frac{\partial}{\partial t}(\rho \boldsymbol{U}) + \nabla \cdot (\rho \boldsymbol{U} \otimes \boldsymbol{U}) = -\nabla p + \nabla \cdot \boldsymbol{\tau} + \boldsymbol{b} \qquad (6)$$

$$\frac{\partial}{\partial t}(\rho e) + \nabla \cdot (\boldsymbol{U}(\rho e + p)) = \nabla \cdot (k \nabla T) \qquad (7)$$

Here, p denotes pressure, $\boldsymbol{b}$ body forces, $\boldsymbol{\tau}$ the viscous stress tensor, and e the total specific energy. Presently, both phases are considered as Newtonian fluids. The effects of surface tension are considered at the interface between the gas phase and ambient liquid. The pressure jump across the liquid-gas interface is modeled with a body force in the momentum equation according to the Continuum surface force model (Brackbill et al., 1992). The liquid phase is modeled as compressible according to the Tait's equation of state, whereas the gas phase is considered as ideal gas.

Numerical model setup

Expansion of an initially stable microbubble (initial radius R_0=1.1 μm) is achieved by over pressurizing the bubble interior (initial bubble pressure 1.96×10^8 Pa) in comparison to the ambient pressure (p_∞=101,325 Pa). The ambient liquid temperature is set to 293.15 K. A bubble is initiated between d_b=1.5 μm and 15 μm (increment of 1.5 μm) away from the wall, which in the present case amounts to the non-

dimensional bubble-wall distance γ=d_b/$R_{r,max}$ between 0.087 and 1.02 (increment of ≈ 0.1). The gas phase is considered as air and the ambient liquid as water. The corresponding material parameter are given in Table 1. Simulations are done in axial symmetry with an orthogonal grid of uniform spacing in vicinity of the bubble (Δx=44 nm, $R_0/\Delta x$=25, $R_{r,max}/\Delta x \approx 370$), chosen based on grid and time-step independence analysis in previous research (Zevnik and Dular, 2022, 2021, 2020). In addition, solution convergence for the present case was additionally controlled for the case with $\gamma \approx 0.2$. For the maximum jet speed (see Fig. A6c), the error at the chosen resolution towards the grid independent solution was estimated at -7.4%. The grid independent solution was calculated according to the Richardson interpolation, from the results obtained by three sequential simulations with resolutions of roughly 200, 400, and 800 computational cells per maximum bubble diameter. The grid spacing gradually coarsens towards the computational domain edges and the total number of cells at the chosen resolution is in the order of half a million. Computational time step is set according to the Courant–Friedrichs–Lewy condition with the maximum cell Courant number of 0.2. Boundary conditions at the end of the computational domain were set to wave non-reflecting pressure outlet (p_∞=101,325 Pa, T_∞=293.15 K) and no-slip condition is considered at the wall. More details regarding the employed numerical model and setup can be found in our previous work (Zevnik and Dular, 2022).

Attached cell model

Expanding and collapsing cavitation microbubble induces a temporally and spatially variable flow field in the ambient liquid, which exerts hydrodynamic loads on nearby wall-bound cells. Under the assumption of a spherical cell shape, we can estimate the hydrodynamic drag force $\boldsymbol{F}_d$, which can be for an attached spherical cell of radius R_c written as

$$\boldsymbol{F}_d = \frac{1}{2} \rho_l \pi R_c^2 C_d \bar{\boldsymbol{u}} |\bar{\boldsymbol{u}}|. \qquad (8)$$

Here, $\bar{\boldsymbol{u}} = \bar{\boldsymbol{u}}(t, r_c)$ is local flow velocity at the location of the cell r_c. Since the presence of cells is not actually considered in the bubble dynamics model, the height of bacterial cells h_c above the wall is not guaranteed to be greater than the numerically obtained liquid film thickness formed between the bottom bubble surface and the wall, due to the small standoff bubble-wall distances γ considered. The effective flow velocity is thus determined as
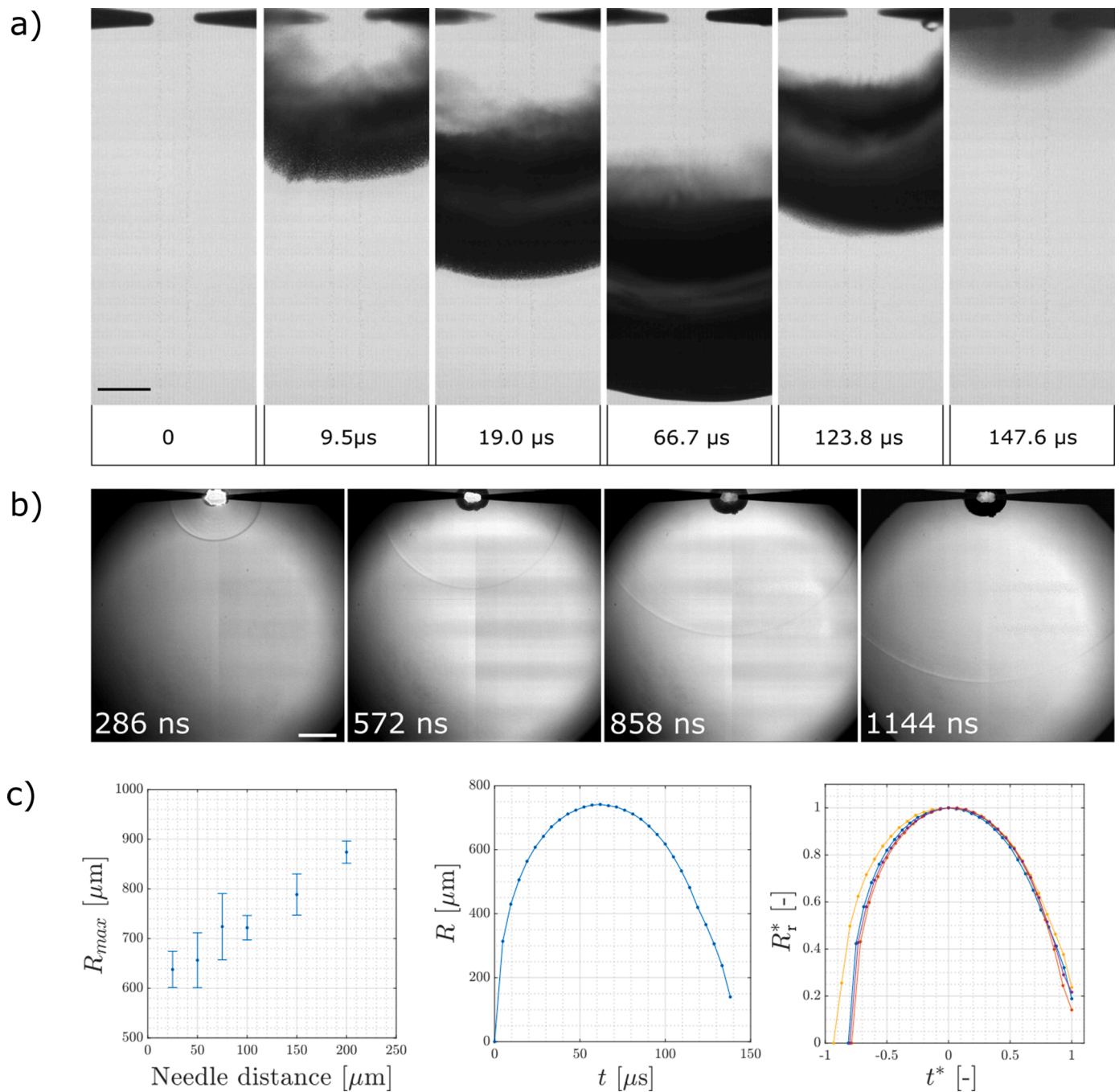
Fig. A1. (**a**) Image sequence after spark discharge. The spark discharge between needles (75 µm standoff distance) creates vapor void which after the initial bubble growth collapses. Scale bar 100 µm. (**b**) Generation of shockwave during high voltage discharge bubble. Scale bar 400 µm. Shockwaves were observed with Kirana 7 M high speed camera and laser pulses as a light source. (**c**) Left: The effect of needle stand-off distance on bubble maximum radius (R_{max}) during spark discharge bubble collapse. Increasing the stand-off distance between needles increases maximum collapse radius. Error bars represent SD ($N = 5$). Middle: bubble radius development during spark discharge at needle stand-off distance 75 µm. Right: Temporal development of non-dimensional bubble radius R_r^* with non-dimensional time t* (see Appendix C) for 4 experimental cases.

$$\overline{\boldsymbol{u}}(t, r_c) = \frac{1}{h_c} \int\limits_{z=0}^{z=h_c} \alpha_l \boldsymbol{u}(t, r_c, z) dz, \qquad (9)$$

where only velocity field of the liquid phase is considered to better represent the actual experimental conditions, where the bubble is expected to overlay the cells, rather than engulf them. The drag coefficient C_d can be calculated according to the Kaskas equation (Kaskas, 1964) as:

$$C_d = \frac{24}{Re} + \frac{4}{\sqrt{Re}} + 0.4, \qquad (10)$$

which is valid for Reynolds numbers $Re < 2 \cdot 10^5$. Reynolds number is presently defined as

$$Re = \frac{2R_c \rho_l |\boldsymbol{u}|}{\mu_l}. \qquad (11)$$

Presently, cells are considered as spheres with radius of $R_c = $
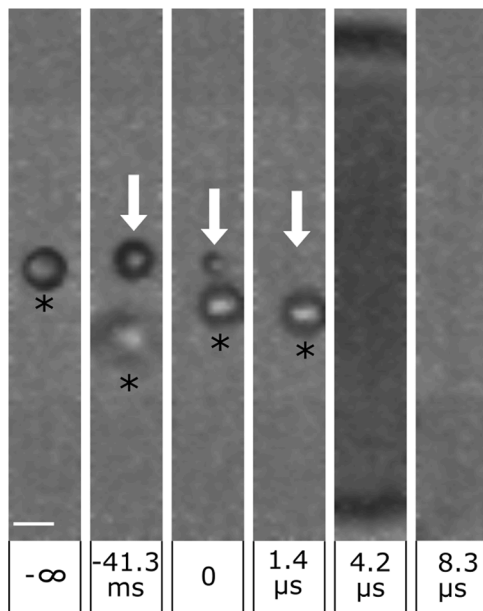
Fig. A2. At -∞ magnetic microbead (*) was positioned with an optical tweezers at a desired location. At -41.3 ms stable nucleation microbubble was generated with the laser pulse (arrow). The nucleation microbubble was stable on microsecond timescale. At time zero the nucleation microbubble underwent contraction due to local focusing of a tension wave induced with spark discharge. At 1.4 µs, the bubble maximally compresses followed by violent expansion at 4.2 µs ($R_{r,max}$). Please note different time scales for the nucleation microbubble (milliseconds) and cavitation microbubble expansion/collapse (microseconds). Scale bar 3 µm.

$\left(\frac{1}{8}d_c^3 + \frac{3}{16}d_c^2(l_c - d_c)\right)^{\frac{1}{3}} = 0.45 \pm 0.06$ µm. Here, $l_c = 1.44 \pm 0.25$ µm and $d_c = 0.63 \pm 0.06$ µm ($N = 30$) denote the actual bacterial cell length and diameter. The latter also corresponds to the bacterial cell height h_c above the wall. The expression for cell radius R_c is obtained from computing the equivalent radius of the actual bacterial cell volume, assuming a spherocylindrical cell shape.

2.4. Cell event probability model

The relation between the exerted peak hydrodynamic force and the probability of single cell event occurrence (detachment, cell death) was quantified by fitting the obtained data to the cell event probability model. The latter is described by a piecewise function with three coefficients. The main relation between the chosen load metric and cell event probability is characterized by a power law function, where the coefficients are set up in a way to represent the lower threshold load, upper threshold load, and the corresponding load exponent. The cell event probability at the peak hydrodynamics force F_{max} is fitted according to the following piecewise function:

$$P_{event}(F_{max}) = \begin{cases} 0, & |F_{max}| < F_{lth}, \\ \dfrac{|F_{max}|^{\beta_F} - F_{lth}^{\beta_F}}{F_{uth}^{\beta_F} - F_{lth}^{\beta_F}}, & F_{lth} \le |F_{max}| \le F_{uth}, \\ 1, & F_{uth} \le |F_{max}|. \end{cases} \quad (12)$$

Here, F_{lth} and F_{uth} correspond to lower and upper peak force threshold. The former can be understood as a threshold for the possible occurrence of the considered cell event ($P_{event}(F_{max}) \approx 0$), whereas the latter represents the upper threshold force, above which the considered cell event is likely to occur for the vast majority of cells ($P_{event}(F_{max}) \approx 1$). β_F is a third fitting coefficient and denotes the force exponent. A similar model is employed to characterize cell event probability in relation to the peak
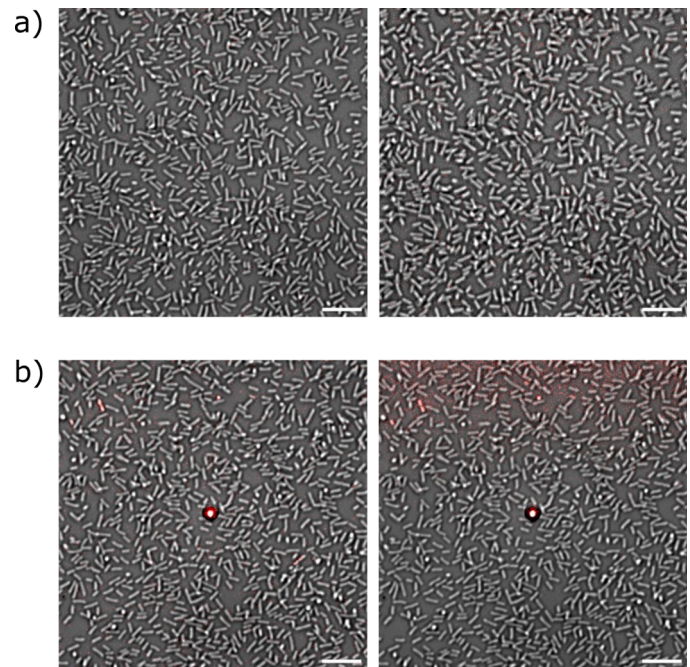

Fig. A3. Effect of spark discharge bubble and shockwave propagation on observed monolayer of bacterial cells (a). Left image shows cells before generation of spark discharge, right image shows cells after spark discharge, with no evident cell detachment nor bacteria staining with PI dye (dead cells). Scale bar represents 10 µm. b) Effect of nucleation microbubble generation on bacterial cells (a). Left image shows magnetic bead in the middle of the image before nucleation microbubble generation, right image shows cells after nucleation microbubble generation. Magnetic bead remained at similar position, with no evident cell detachment or bacteria staining with PI dye (cell death). Scale bar represents 10 µm.

wall shear stresses τ_{max}. Model fitting was performed using a non-linear least squares method along with a thrust-region algorithm. A global fit was performed for each load metric-cell event pair (4 pairs in total).
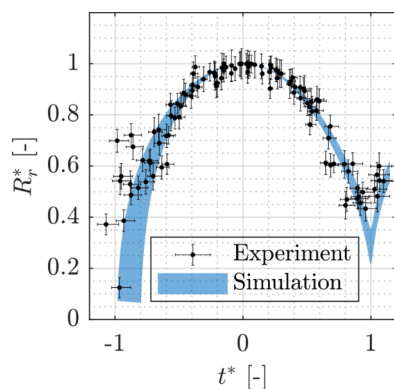
3. Results

3.1. Experimental observations of the interaction of a single cavitation microbubble with a bacterial cell

Upon a µs laser pulse, local heating generated a micrometer sized stable nucleation microbubble with a median radius of 1.1 µm ($N = 15$). The lifespan of a nucleation microbubble was in the order of milliseconds to seconds and the nucleation microbubble formation had no effect on nearby bacterial cell adhesion and viability (Fig. A3). The formation of an unstable cavitation microbubble (Fig. 3a) was triggered by shock waves (Fig. A1) induced by a remote spark discharge (approximately 3 mm from the nucleation microbubble site). The initially stable nucleation microbubble first underwent a contraction upon shock wave propagation, which was then followed by an explosive microbubble expansion (during ~ 1.4 µs) due to the focusing of a tensile wave. The induced cavitation microbubble expanded in size to the median maximum radius of 15.4 µm ($N = 15$). During a rapid cavitation microbubble collapse (~ 1.4 µs), we were able to observe a microjet formation. The latter was directed towards the rigid surface as indicated by the inner dark annulus on Fig. 3a. The effect of a single microbubble collapse on a monolayer of attached bacterial cells is shown in Fig. 3b. The bacterial cells were initially homogenously distributed over the entire field of view (cell density was 0.15 ± 0.03 cells/µm^2) and the magnetic beads were positioned at different locations in the vicinity of the bacterial cells by optical tweezers. After exposure to microbubble collapse, one can observe an area of detached bacterial cells in the center

a)

b)
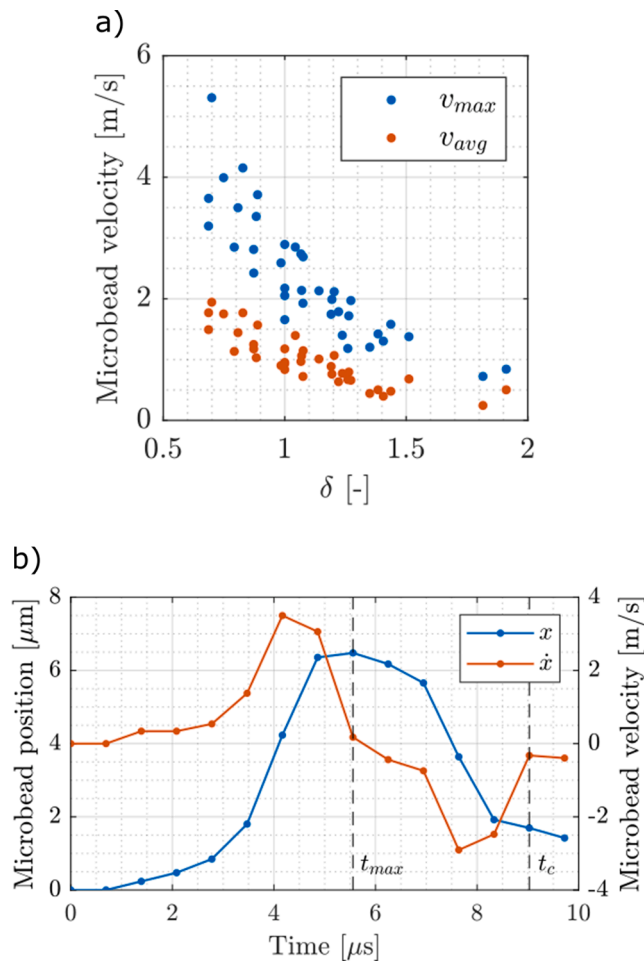
Fig. A4. Microbubble-induced flow field causes movement of a nearby silica bead. (**a**) Experimentally obtained peak (blue dots) and time-averaged (orange dots) microbead velocities ($N = 37$) show a non-monotonic decreasing trend with δ. (**b**) Microbead position (blue, left ordinate) was tracked during a microbubble event, from which the corresponding particle velocities (orange, right ordinate) were obtained by central differencing. Time series is shown for a sample case with $R_{r,max}$=18.7 μm, δ=0.70, and γ=0.22. The times of maximum bubble size t_{max} and bubble collapse t_c are denoted by a vertical dashed line. Temporal resolution is 0.7 μs.


Fig. A5. Temporal development of microbubble radius R_r^*. Data is given in non-dimensional form. Experimental results are denoted by black dots, handlebars represent the estimated measurement errors (± 2 px=± 0.67 μm). Results of numerical simulations are given in a blue fill, which represents the min-max envelope of the obtained numerical microbubble radius progression.

of the projected cavitation microbubble radius. Furthermore, the zone of detached cells is surrounded by an annulus of still attached but damaged bacterial cells. The fluorescence image (red pseudo-colored bacteria) shows cells with a compromised cytoplasmic membrane. The latter resulted in the uptake of membrane impermeable PI fluorophore, indicating cell death. The dashed circle represents the projected maximum microbubble radius $R_{r,max}$ obtained from high-speed camera imaging. Based on experimental results and image analysis we could categorize individual bacterial cells as either detached, attached but dead, or not affected (Fig. 3c). The area of damaged bacterial cells is similar to the projected maximum microbubble size. Due to high-speed photography constraints (temporal resolution 0.7 μs, spatial resolution 3 px/μm), only cavitation microbubbles with the maximum expansion radius above 10 μm were used in further statistical analyses. Nevertheless, it has to be stressed that the presented method also allows for a reproducible generation of smaller cavitation microbubbles. In the most cases, a single cycle of bubble oscillation was observed (as shown in Fig. 3a). However, in rare cases, the microbubble underwent an additional oscillation phase, which could lead to an exaggerated estimate of the effectiveness of the primary bubble. However, the secondary oscillations occurred within the area of maximum bubble size where there is a high probability that cells are already detached or damaged from the primary oscillation cycle. Additionally, it is important to note that in the absence of the stable nucleation microbubble, the spark discharge did not induce cavitation events at the magnetic bead nor had any effect on bacterial cell adhesion and viability in the observed experimental volume (Fig. A3). Also, according to the high-speed microbubble shape visualizations the presence of magnetic microbeads did not affect the microbubble dynamics near the solid wall.

3.2. Mechanisms that cause bacterial cell detachment and damage

To gain a mechanistic insight into the microbubble-bacteria interaction, numerical simulations of near-wall microbubble dynamics were performed, from which bubble shape evolution and the resulting flow field were obtained. These results were then used to determine the hydrodynamic forces on nearby wall-bound bacterial cells (Fig. 4). The obtained numerical results reveal two distinct characteristic modes of microbubble collapse, which primarily depend on the value of the microbubble-wall distance parameter γ, presently defined as a ratio of the initial bubble-wall distance and the maximum projected microbubble radius (Fig. 2). Both bubble collapse modes include a uniaxial jet formation towards the wall. However, the characteristics of the developed jets vastly differ between both modes. For microbubbles in extreme vicinity of the wall (γ≲0.3) a very fast and thin jet towards the wall is developed (Fig. 4a), with the peak jet velocity well above 1000 m/s (between 1200 and 1400 m/s) and a normalized jet radius ($R_{jet}/R_{r,max}$) of 0.021±0.001. On the other hand, for microbubbles with γ≳0.4 a commonly recognized classical jet can be observed (Fig. 4b), with a normalized radius of 0.30±0.02 and peak velocities between 56 and 75 m/s (64±8 m/s).

The resulting peak wall shear stresses and hydrodynamic forces during a single cavitation event are given in Fig. 4c, which shows high spatial variability and non-linear dependence on the microbubble-cell distance δ. One can observe an increase in the width of the shaded area (min-max envelope) for δ<0.2, which points towards a highly variable magnitude of peak microbubble-induced mechanical loads in the region of the jet impact. This can be attributed to the fact that different microbubble jetting modes can occur along the bubble-wall distance parameter γ (Fig. 4a, b). Peak magnitudes of the hydrodynamic forces and wall shear stresses at δ <0.1 can locally reach ten micronewtons and a few megapascals, respectively. The occurrence of peak loads coincides with the time of jet impact and subsequent outward radial flow along the wall. The peak loads, however, are highly transient (tens of nanoseconds) as their duration is roughly two orders of magnitude shorter than the cavitation microbubble lifetime (few
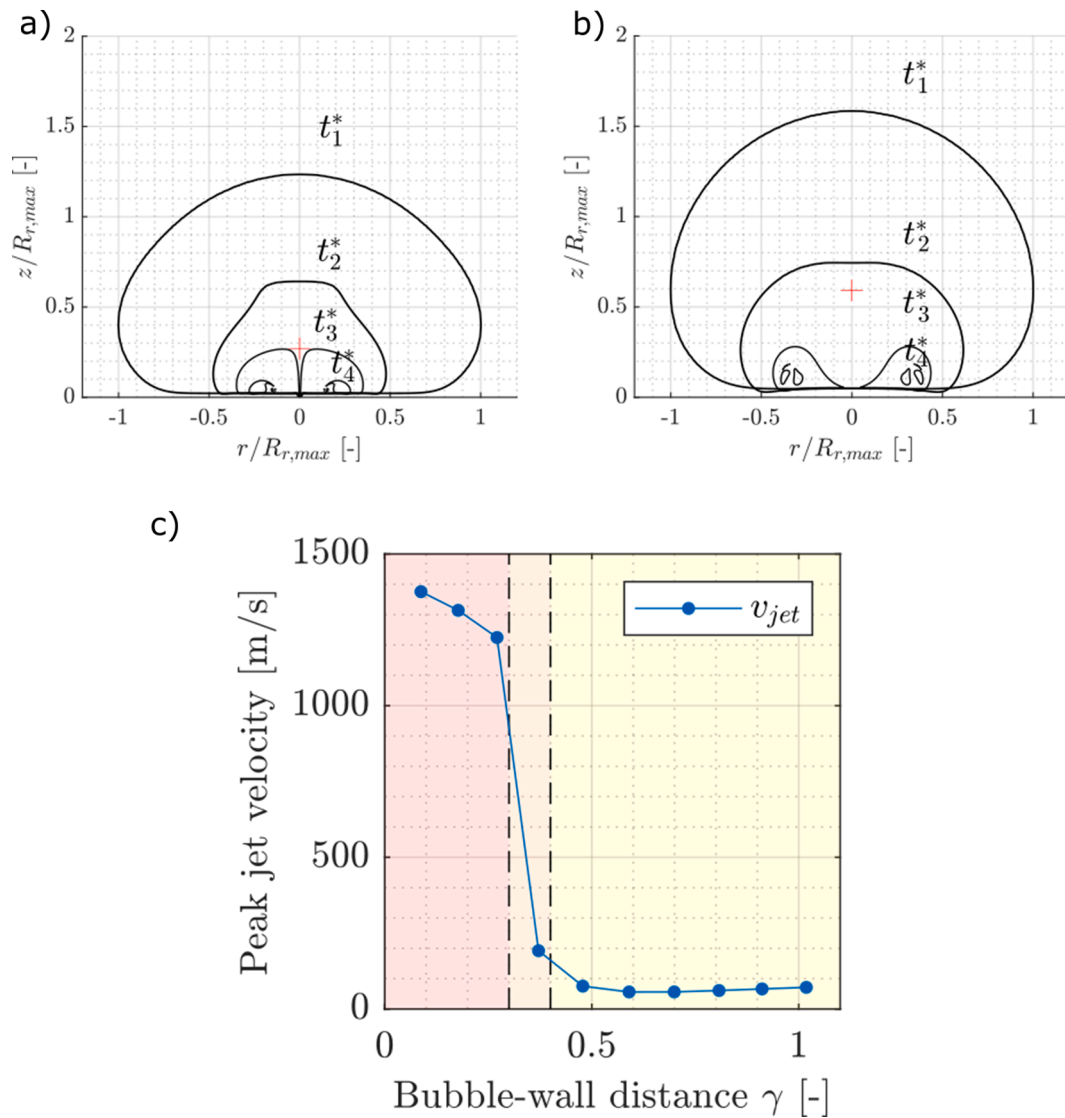
Fig. A6. Numerical modeling of cavitation bubble. (**a**) Temporal progression of the microbubble shape (side view) as predicted by numerical simulation for $\gamma=0.27$, which shows a fast thin jet formation, typical for microbubble collapse in close vicinity of a rigid boundary ($z = 0$). Red cross mark corresponds to the center of the initial microbubble. Contours correspond to the maximum microbubble size ($t_1^*=0$), half the maximum size ($t_2^*=0.895$), followed by a fast thin axial jet formation with touchdown ($t_3^*=0.964$), and collapse of the remaining toroidal microbubble ($t_4^*=1.004$). (**b**) Temporal progression of the microbubble shape (side view) as predicted by numerical simulation for $\gamma=0.59$, which shows a commonly recognized axial jet formation towards a rigid boundary ($z = 0$). Red cross mark corresponds to the center of the initial microbubble, Contours correspond to maximum microbubble size ($t_1^*=0$), half the maximum size ($t_2^*=0.831$), jet formation and touchdown ($t_3^*=0.961$), followed by collapse of the remaining toroidal microbubble ($t_4^*=1.008$). (**c**) Peak jet velocity (blue circles) in relation to microbubble-wall distance parameter γ, as predicted by numerical simulations. The obtained regions of the identified microbubble jetting modes are denoted by a colored fill, with the estimated boundaries (black dashed lines, orange fill) at $\gamma\approx0.3$ and 0.4 for a fast thin jet (red) and classical jet development (yellow), respectively.

microseconds). Additionally, the loads decay quickly with the distance from the center of the jet, and cells at the distance of the maximum microbubble radius ($\delta=1$) are subjected to the peak local shear stress and hydrodynamic forces of 20 kPa and 70 nN, which is several orders of magnitude smaller than in the center of the jet. The results of the simulations are in line with the present experimental observations of bacterial cell detachment and destruction, as the formed crater of detached cells in the center of the jet impact zone indicates the highest shear stresses and hydrodynamic forces.

3.3. Effectiveness of a cavitation microbubble to eradicate wall-bound bacterial cells

Probabilities of the two main identified bacterial cell outcomes, cell detachment and cell death, are presented in Fig. 5. Shown results are based on the data gathered from fifteen experimental cases, where maximum radii of cavitation microbubbles and positions of *E. coli* cells were documented in accordance with the definition of the microbubble – cell distance δ (Fig. 2). A very high likelihood (almost 100%) of cell detachment can be seen for cells located directly under the center of an imploding microbubble ($\delta \leq 0.2$). This was already noted before from the microscopic images in the form of area without bacterial cells (Fig. 3b). As high probability for cell detachment directly under the center of microbubble, cell death is presented for values only above $\delta>0.2$. With $\delta>0.2$ cell detachment probability exponentially decreases, reaching 25% probability at $\delta=1$ and 10% for $\delta=1.5$. Due to inability to track detached cells, *E. coli* viability was determined from the cells that remained attached (Fig. 5b). We can observe that cell death probability exponentially decreases with δ and is practically null for $\delta > 1$. The results suggest that it is easier to detach bacterial cells than to damage
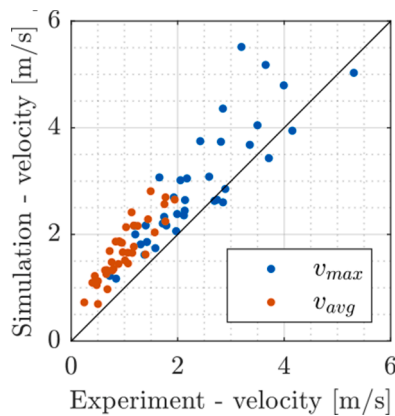
Fig. A7. Microbubble-induced velocity field. A comparison between experimental and numerical results shows a good level of agreement for both velocity metrics: peak microbead velocity v_{max} (blue dots, RMSE=0.79, R^2=0.73, N = 37) and time-averaged microbead velocity v_{avg} (orange dots, RMSE=0.75, R^2=0.77, N = 37).

them as the former outcomes shows consistently higher probabilities along δ (i.e., the median probability for bacterial cell detachment decreases towards only after δ > 2, whereas cell death is decreased toward zero already at δ > 0.8).

3.4. Required mechanical loads for removal and eradication of bacteria on a temporal scale of a single cavitation microbubble event

The relation between the exerted peak mechanical loads and the probability of identified cell outcomes is given in Fig. 6. The obtained experimental and numerical results were fitted to a piecewise power law model (Materials and Methods, Section 2.4 – Cell event probability model). The obtained model parameters (Table 2) can be understood as the threshold mechanical loads for the possible outcome of cell detachment or death, when subjected to high frequency mechanical perturbations on a nano- to microsecond time scale. The lower threshold corresponds to the bound below which a certain cell outcome is highly unlikely ($P \approx 0$), whereas the upper threshold denotes the bound above which a cell outcome has a very high likelihood of occurrence ($P \approx 1$). Presently, we observed a very high likelihood of *E. coli* bacteria detachment at peak hydrodynamic force of 0.8 ± 0.1 μN and cell death at 1.2 ± 0.5 μN. These values translate to the microbubble-cell distance for a highly probable outcome of cell detachment on the interval of δ = [0, 0.4], and δ = [0, 0.35] for cell death. In certain applications, especially in medicine, a similar question is usually framed the other way around – at what forces or bubble-cell distances can we still expect the cells to remain viable. In our case, cells are not expected to get detached or damaged when peak forces are below 14±4 nN and 52±14 nN. Additionally, microbubble collapse mode (fast thin jet versus classical jet) did not affect the obtained cell event probability distribution along δ (Appendix D), which suggests that *E. coli* cell detachment or death is independent of the microbubble jetting mechanism.

4. Discussion

Downscaling of the cavitation process to a single cavitation microbubble and study of its interaction with a bacterial cell has not been performed yet. In this study, spatio-temporal control of a single cavitation microbubble combined with numerical analysis provided unprecedented mechanistic insight into hydrodynamic forces and shear stresses that affect individual bacterial cells during a single cavitation microbubble event. We present a direct observation of bacterial cell response to high frequency mechanical perturbations spanning the time domain from nanosecond to microsecond.

High frequency perturbations on bacterial cells have been used with mixed success for antibacterial purposes in the past (Salmen et al., 2018; Wietzikoski Lovato et al., 2018). For example, exposure of *S. epidermidis* and *S. aureus* to high frequency electromagnetic fields mostly produced no statistically significant decrease on bacterial growth. On the other hand, exposure of *P. aeruginosa* to electromagnetic fields at 900 MHz led to a significant reduction in growth rate, while 1800 MHz had insignificant effect. The effects have been attributed to temperature gradients and the formation of reactive oxygen species (ROS). Although similar physico-chemical effects on bacteria have been proposed for cavitation we argue that in the case of single microbubble cavitation event high frequency mechanical effects on bacterial cells are far more significant than temperature and ROS.

The effects of a single microbubble collapse are highly transient as single microbubble growth and collapse is completed in approximately 5 μs. Those effects are not as sustained as in the case of high frequency electromagnetic fields or high frequency ultrasound cavitation. For example, Yasuda et al. (2016) have used high frequency focused ultrasound (1 MHz) pulses to generate ROS, but for an efficient ROS generation they had to use a repeated sequence of high intensity pulses for 5 min. In the case of ultrasound cavitation, it is known that higher production of ROS is expected at high frequency ultrasound (100 kHz and above) as less energy during the bubble collapse translates into shockwaves and the number of bubble collapses is increased (Mason et al., 2011; Yusof et al., 2016). This suggests that during the single cavitation event a probability for ROS generation is very low. Due to high reactivity of ROS species, it would be technically very challenging to detect their presence during the single cavitation event, although the generation of ROS cannot be completely excluded. On the other hand, physical mechanisms that accompany cavitation such as high local temperatures (Suslick et al., 1999), strong shear flows (Zupanc et al., 2014), jets (Dular et al., 2019), shock waves (Petkovšek et al., 2020), rapid pressure drop (Šarc et al., 2016) and supersonic flow (Shamsborhan et al., 2010) are much more likely during a single cavitation event. The controlled single microbubble experiment together with computational simulations provides an opportunity to determine which mode of cavitation is more significant to bacterial inactivation.

During a microbubble collapse the temperature within the microbubble may reach peak values of several thousandths Kelvin (Suslick et al., 1999). However, these are short lived and spatially confined to the center of the collapsing microbubble. From our previous numerical research, it follows that thermal load on bacteria during a single microbubble event could only be relevant in cases when the collapsing microbubble remains in the direct proximity of the cell surface (Zevnik and Dular, 2022, 2021, 2020), as the thermal boundary layer is thin in comparison to the maximal bubble size. In the case of non-attached microbubbles, the temperature changes at the location of a bacterium are in fact negligibly small, and well below the threshold for bacterial death (Mitsuzawa et al., 2006). The same, however, cannot be said for compressive and shear loads. The experimental and numerical results suggest that the main contributing damaging mechanism for wall-bound bacteria is a microjet formation towards the wall. Upon impact, the jet changes flow direction and flows radially outwards along the wall, causing high local pressures and shear forces on the attached cells. Looking at the maximum calculated values along δ, we can observe shear stresses in the order of a few megapascal and the resulting hydrodynamic forces as high as ten micronewtons.

The presently obtained results point toward the jet impact and its outflow along the wall as the primary mechanism that causes wall-bound bacterial cell detachment and death, when a single near-wall microbubble event is considered. Nevertheless, we presently cannot exclude the possibility of a synergistic effect of other potentially damaging mechanisms, such as free radicals and shock waves. The reasoning for outlining the jet as the primary mechanism is as follows; First, a microbubble event causes cells either to detach from the wall, die, or remain unaffected. The regions of detached cells exhibit round

shapes and are surrounded by annular-shaped areas of attached but dead bacterial cells. Centers of both regions are tightly related to the bubble center, which also corresponds to the jet center (see Figs. 3b and 3c). These findings point towards a mechanism that can be characterized by axial symmetry with its center at the bubble (jet) center. Second, the results imply that cell detachment is practically guaranteed for δ<0.3, which is followed by a monotonic and gradually decreasing trend of cell detachment probability with radial distance δ from the bubble (jet) center (see Fig. 5a). A similar trend was also observed for cell death (see Fig. 5b). Similar non-linearly decreasing trends are obtained for both bubble-induced load metrics, peak hydrodynamic force and wall shear stress, obtained from numerical simulations. Furthermore, the occurrence of peak calculated loads corresponds to the time of jet impact and its radial outflow along the wall. Third, the radial position of the toroidal bubble collapse is obtained to range between $0.23 \leq \delta \leq 0.36$ (see non-dimensional Rr* at non-dimensional t*=1 in Fig. A5 and bubble shapes at t4* in Figs. A6a and A6b). We do not exclude the toroidal bubble collapse as a contributing mechanism for causing bacterial cell detachment and death, however, based on the observed trends of cell outcomes with radial distance δ from the bubble center, we find it highly unlikely to be the primary damaging mechanism. Furthermore, our previous research (Pandur et al., 2022; Zevnik and Dular, 2022, 2021) points toward a conclusion that high pressure and shock waves of magnitude characteristics of bubble collapse are not being sufficient to cause bacterial cell damage. The reason for this is a relatively high stability of bacterial cell envelopes to compressive loads, their high compliance and thus a similar acoustic impedance to water, which renders them almost invisible to weak shock waves. Nevertheless, an important note to add here is that we expect the intensity of bubble collapse to play an important role in this regard, which could lead to different conclusions with other considered bubble collapse scenarios than the ones considered in the present study. For example, Reuter et al. (2022) have just recently observed that cavitation erosion of harder materials occurs only for laser-induced bubble collapses at close stand-offs below γ≈0.2, where a shock wave self-focusing mechanism develops. However, the latter results from non-axially symmetric bubble collapse causes the damage to be localized to a narrow spot away from the central axis, which is not the case in the presently obtained results.

As observed, there are three possible outcomes for bacteria after a single cavitation event. Bacteria are either detached, remain attached but dead, or remain attached and viable. The probability for cell detachment and damage exponentially decreases with bubble-cell distance. Similar effects were observed for attached eukaryotic cells (Gac et al., 2007; Hellman et al., 2008; Jasikova et al., 2019; O'Connor et al., 2021; Ohl et al., 2006; Rau et al., 2006; Zhou et al., 2012). For a single cavitation event, we determined hydrodynamic force for bacterial detachment to be in the range from 14 nN to 0.8 μN. The detachment probability increases with hydrodynamic force and is very likely above 1 μN ($P = 1$). Detachment of *E. coli* from a PLL coated glass substrate was measured independently with FluidFM method by Potthoff et al. (2015), who measured the detachment force of 14 nN per cell. This is comparable to our detachment threshold force. The threshold force for cell death was higher than for detachment (1.2 μN). This is in line with the reported bursting force of 3.6 μN for the exponential grown *E. coli* (Shiu et al., 1999).

The highest mechanical stress was calculated at the projected center of microbubble collapse due to jet formation, which is consistent with the experimental observation, where all bacteria detached at the center of the projected cavitation microbubble. The obtained peak wall shear stress of 145 kPa during the single cavitation event corresponds to the one reported by Zeng et al. (2018), where they report wall shear stresses of 100 kPa after the jet impact. Numerical results revealed two distinct modes of microbubble collapse – a classical jet (Dular et al., 2019) and a fast, thin jet (Koch et al., 2021; Lechner et al., 2020, 2019; Reuter and Ohl, 2021), depending on the microbubble-wall distance. We were unable to experimentally observe a fast needle-like jet due to the limited

spatial-temporal resolution of the high-speed camera, although observation in bigger cavitating bubbles were recently reported (Koch et al., 2021; Lechner et al., 2020; Reuter and Ohl, 2021). Despite different jetting modes, bacterial cell detachment nor viability did not significantly differ between the two jetting modes. This finding can be further explained by the obtained numerical results presented in Fig. 4c, where peak bubble-induced loads are shown. There, we can observe that the min-max envelopes of both load metrics exhibit very high variation (beyond an order of magnitude) across γ in the region directly below the bubble center (δ<0.2), which can be attributed to vastly different microbubble collapse and jetting dynamics. However, moving further away from the bubble center, we can observe a relatively narrow span of the min-max envelope (up to a few ten percents for δ>0.5) between all considered cases (0.15≤γ≤0.58). This implies that the peak loads on cells are of similar magnitudes across both identified bubble jetting modes, i.e., fast thin jet and classical jet, when cells are positioned sufficiently far away from the bubble center (δ>0.5). One additional important thing to consider is the fact that with δ<0.3, virtually all cells were either detached or remained attached to the wall but died (see Fig. 5). From that one can deduce that even bubble collapse with classical jet formation causes high enough loads to affect bacterial cells.

The results of this study imply an intimate relation between the bacterial cell and a cavitation microbubble. Only when the two are in contact or in very close proximity, a bubble has an effect on the bacterial cell. The detrimental effect of cavitation on bacterial viability and attachment is spatially confined to the center of the projected cavitation microbubble. This suggests that a vast majority of cavitation events in the suspension will go unnoticed by bacteria. Of course, one should not neglect micro and macro streaming of the fluid induced by cavitation events, which is expected to have a cleaning effect (Verhaagen and Fernández Rivas, 2016). While the results are strictly speaking valid only for *E. coli,* a Gram-negative bacterium, recent numerical simulations by Zevnik and Dular (2022) revealed that the difference in peak cavitation forces felt by Gram-negative and Gram-positive bacteria is only 20–30%. However, this needs to be experimentally verified. The present research focused on a relation between cavitation microbubbles and attached cells, which renders the findings as less applicable to free floating planktonic cells in suspensions. However, still most of the bacterial cells in environment are present in a group of cells (i.e., biofilms or flocs) or at least are embedded in complex biological extracellular matrix (Costerton et al., 1995; Guasto et al., 2012; Hall-Stoodley et al., 2004; Sretenovic et al., 2017). All these cases could cause cavitating microbubbles to from characteristic jets toward bacterial cells, as is also true in the presented paper. Examples of a complex medium are wastewater and activated sludge, where enormous amount of biological material needs to be treated. The threshold cavitation forces for embedded cells in biomatrix (e.g., biofilms) are currently unknown and could be higher due to increased biofilm stress resistance compared to monolayer (Costerton et al., 1995; Hall-Stoodley et al., 2004; Simunič et al., 2020). However, if one is interested in inactivation of bacteria, the majority of cavitation events will not reach its target. Due to the statistical nature of the cavitation, increasing the number of "micro" cavitation events should increase the likelihood of the direct contact between the bacterial cell and the cavitation bubble. Therefore, to increase efficiency of cavitation for bacterial killing purpose one should aim to increase the density of microbubbles in the suspension. Yet, the effectiveness of different sized cavitation bubbles (micro- and macro scale) on cells is still not exploited and could have an effect of effectiveness as suggested by Zevnik and Dular (2022). Determining the bacterial threshold mechanical loads enables quantitative assessment and further optimization of novel surface and water treatment technologies to provide more efficient and chemical free processes of water treatment.

On the other hand, the ability to produce and manipulate single cavitation microbubbles could have far more reaching consequences for the future technologies. For example, a reliable production of single

cavitation microbubbles could be used in medicine as a high precision surgical tool with the ability to mechanically remove problematic cells with the minimal collateral damage. The use of high energy quanta released during the single cavitation event could also be used in nano-technology for targeted delivery of molecular payloads or for nano-patterning of biotic and abiotic surfaces.

Declaration of Competing Interest

The authors declare that they have no known competing financial interests or personal relationships that could have appeared to influence the work reported in this paper.

Data availability

Data will be made available on request.

Appendix A. Extended experimental setup

Experimental setup is assembled out of two cavitation bubble events: i) high voltage spark discharge bubble collapse on millimeter scale and ii) nucleation microbubble collapse on micrometer scale.

High voltage spark discharge is positioned in the experimental chamber via Tungsten micrometer sized needles, where bubble collapse dynamics can be seen in Fig A1. Bubble growth and collapse occurs in tenths of μs – example in Fig A1a at stand-off distance 75 μm: t_{max}=66,7 μs with R_{max}=720 μm). Generation of shockwaves can be observed at the beginning of spark discharge at the beginning of the plasma formation (Fig. A1b). Estimated propagation of shockwaves was approximately 1700 m/s. Manipulation of discharge bubble dynamics can be done via change od stand-off distance between needles. The effect of needle stand-off distance on bubble maximum radius (R_{max}) during spark discharge bubble collapse is shown in Fig. A1c left figure. At 25 μm stand-off distance bubbles with R_{max} 638±36 μm can be produced. Increasing the stand-off distance to 200 μm between the needles increases maximum bubble radius to R_{max} 874±22 μm. To directly compare different experimental and numerical results, bubble radii and the corresponding times were transformed into their non-dimensional form as $R_r^* = \frac{R_r}{R_{r,max}}$ and $t^* = \frac{t-t_{max}}{t_c}$, respectively. Temporal bubble size dynamics shows symmetrical bubble growth and collapse, where initial bubble growth shows some discrepancies as ambient pressure oscillations are present.

Generation of single microbubble cavitation started with short laser pulse on magnetic microbead to produce nucleation microbubble (Fig. A2). Nucleation microbubble was located on the surface of the magnetic microbead or was detached from surface of the microbead. Next, the high voltage spark discharge was released to produce cavitation bubble, and propagation of pressure waves. Lag time between generation of nucleation bubble and spark discharge bubble was approx. between 50 and 100 ms. This lag time didn't have influence on microbubble collapse as nucleation microbubble lifetime was in the range of hundredths of miliseconds.

Surface attached bacterial cells were homogenously distributed on PLL coated glass slide (Fig. A3). Bacterial cells formed a monolayer of cells on a glass surface, which were firmly adhered as neither propagation of pressure waves nor generation of nucleation bubble had impact on a nearby cells.

Appendix B. Flow field characterization during a single microbubble event

The experimental chamber was filled with dH$_2$O and magnetic beads as described in Materials and Methods (2.1 Single microbubble generation). Additionally, silica beads (Bang Laboratories, 4 μm diameter) were added to a final concentration of approximately 10^4 beads/ml. The silica beads were accurately positioned at the desired distance from the nucleation microbubble by optical tweezers. High speed imaging was acquired as described in Materials and Methods (2.1 Single microbubble generation). For determination of bead positions on high-speed images, the ImageJ TrackMate plugin was used (Tinevez et al., 2017). LoG (Laplacian of Gaussian) detector was used to automatically detect silica bead, with estimated object diameter 4.2 μm. Furthermore, possible false detection of particle position was manually corrected. For particle tracking, simple linear assignment problem (LAP) tracker was used. Through bead position tracking we could determine bead displacements and velocities induced by a single cavitation microbubble event on a μs timeframe (Fig. A4b). The obtained peak and time-averaged microbead velocities in relation to parameter δ are gathered in Fig. A4a. From there it is clear that microbead velocities show a nonmonotonic decreasing trend along δ bubble-particle distance parameter δ. Additionally, these results were later used a means of validating the employed numerical methodology to resolve fluid flow at the proximity of the microbubble (Appendix C).

Appendix C. Numerical model validation

Near-wall microbubble dynamics

Numerical model of near-wall microbubble dynamics was validated against the experimental results of microbubble shape and size evolution. It is important to note that we refer to the bubble radius R_r as a radius of the outer contour of the bubble shape from the experimental observations, which can be understood as a vertical projection of the bubble shape to the horizontal plane. The maximum bubble radius $R_{r,max}$ from validation experiments varied between 11.0 and 20.5 μm (mean 14.5 μm, $N = 24$) and were obtained by high-speed visualization. The nondimensional bubble-wall distance γ was varied between 0.20 and 0.46 (mean 0.30, $N = 24$). Here, $R_{r,max}$ and t_{max} denote the maximal bubble radius and the corresponding time, and t_c the bubble collapse time. Simulations yield: $R_{r,max}$=16.3 ± 0.5 μm, t_{max}=1.58±0.05 μs, and t_c=1.73±0.07 μs (0.18≤γ≤0.48, increment Δγ≈0.1, $N = 4$). A comparison between the experimentally and numerically obtained cavitation microbubble radii is given in Fig. A5. The non-dimensional projected microbubble radius R_r^* is in good agreement with the experimentally observed radii, especially when one considers the technical limitations at the considered spatiotemporal scales. Some discrepancies can be observed during the initial stages of microbubble expansion ($t^* < -0.9$). This can be explained by the fact that the experimental microbubbles expanded according to the ambient pressure oscillations (local focusing of a tensile wave), which is some cases led to a slower rate of the initial microbubble expansion, depending on the characteristics of the locally induced pressure field. Nevertheless, the present and previous (Zeng et al., 2018) research shows that peak bubble-induced mechanical loads occur during the bubble collapse phase, which is the reason that we consider these discrepancies as still acceptable in the present case.

Visualization of numerically obtained bubble shape evolution revealed two distinct characteristic modes of bubble collapse, which primarily depend on the value of the bubble-wall distance parameter γ (Fig. A6). Both bubble collapse modes include a uniaxial jet formation towards the wall, however, their characteristics (velocity, size) vastly differ between both modes. The occurrence of different jetting mechanisms and the developed jet characteristics are in good agreement with previous studies of near-wall bubble dynamics on larger scales (Lechner et al., 2020). The present experimental setup unfortunately does not allow for evaluation of the developed jet velocities and visualization of fast jets, due to the high-speed visualization constraints (temporal resolution 1.44×10^6 fps, spatial resolution 0.33 μm/px). This has presented as a major challenge even with larger macro bubbles (Reuter and Ohl, 2021). However, the fact that we were unable to observe a jet formation for all experimental cases with γ<0.25 is in line with the occurrence of very fast and thin jets, as predicted by numerical simulations.

Microbubble-induced velocity field

The microbubble-induced ambient velocity field was experimentally characterized by measuring the displacements of silica microbeads as described in Appendix B. The obtained time-averaged and maximum microbead velocities were used to validate the numerical model for the resolution of the near-bubble flow field development. Direct comparison between experimental and numerical results is given in Fig. A7. Overall, the numerical model does seem to overpredict microbead velocities, however, this can be largely attributed the fact that the experimentally obtained results are prone to underestimation due to high-speed photography constraints (high speed camera frame rate of 1.44×10^6 fps yields Δt=0.7 μs). In comparison, the numerical simulations offer much finer temporal resolution with Δt≪0.1 μs.

Appendix D. Statistical analysis

Cell event probability versus δ was fitted to the exponential curve model. Fit of the median cell detachment probability yields $P \propto e^{-2\delta}$, RMSE=0.039, R^2=0.98, while fit of the median cell dead probability versus δ yields $P \propto e^{-4\delta}$, RMSE=0.044, R^2=0.98. For the effect of jetting mechanism on cell detachment and death, a two sample Kolmogorov-Smirnov tests for median cell event probability distributions along δ, with threshold γ of 0.30, yields p-values of 0.77 and 0.71 for cell detachment and death, respectively.

References

Amir, A., Babaeipour, F., McIntosh, D.B., Nelson, D.R., Jun, S., 2014. Bending forces plastically deform growing bacterial cell walls. Proceed. Nat. Acad. Sci 111, 5778–5783. https://doi.org/10.1073/pnas.1317497111.

ANSYS®, 2021. Fluent, Release 2021 R2, help system, fluent theory guide, help system. ed.

Bhuyan, M.K., Soleilhac, A., Somayaji, M., Itina, T.E., Antoine, R., Stoian, R., 2018. High fidelity visualization of multiscale dynamics of laser-induced bubbles in liquids containing gold nanoparticles. Sci. Rep. 8, 1–12. https://doi.org/10.1038/s41598-018-27663-z.

Brackbill, J.U., Kothe, D.B., Zemach, C., 1992. A continuum method for modeling surface tension. J. Comput. Phys. 100, 335–354. https://doi.org/10.1016/0021-9991(92)90240-Y.

Costerton, J.W., Lewandowski, Z., Caldwell, D.E., Korber, D.R., Lappin-Scott, H.M., 1995. Microbial Biofilms. Annu. Rev. Microbiol. 49, 711–745. https://doi.org/10.1146/annurev.mi.49.100195.003431.

Dular, M., Požar, T., Zevnik, J., Petkovšek, R., 2019. High speed observation of damage created by a collapse of a single cavitation bubble. Wear 418–419, 13–23. https://doi.org/10.1016/j.wear.2018.11.004.

Gac, S.le, Zwaan, E., Berg, A.van den, Ohl, C.-.D., 2007. Sonoporation of suspension cells with a single cavitation bubble in a microfluidic confinement. Lab. Chip 7, 1666. https://doi.org/10.1039/b712897.

Gogate, P.R., Pandit, A.B., 2005. A review and assessment of hydrodynamic cavitation as a technology for the future. Ultrason. Sonochem. 12, 21–27. https://doi.org/10.1016/j.ultsonch.2004.03.007.

Guasto, J.S., Rusconi, R., Stocker, R., 2012. Fluid mechanics of planktonic microorganisms. Annu. Rev. Fluid. Mech 44, 373–400. https://doi.org/10.1146/annurev-fluid-120710-101156.

Hall-Stoodley, L., Costerton, J.W., Stoodley, P., 2004. Bacterial biofilms: from the natural environment to infectious diseases. Nat. Rev. Microbiol 2, 95–108. https://doi.org/10.1038/nrmicro821.

Hellman, A.N., Rau, K.R., Yoon, H.H., Venugopalan, V., 2008. Biophysical response to pulsed laser microbeam-induced cell lysis and molecular delivery. J. Biophoton. 1, 24–35. https://doi.org/10.1002/jbio.200710010.

Jasikova, D., Rysova, M., Kotek, M., 2019. Application of laser-induced breakdown cavitation bubbles for cell lysis in vitro. Int. J. Appl. Pharmac. 186–190. https://doi.org/10.22159/ijap.2019.v11s5.T3059.

Kaskas, A., 1964. Berechnung Der Stationaren Und Instationaren Bewegung von Kugeln in Rehunden Und Stromenden Medien (Diplomarbeit). T. U. Berlin, Berlin.

Koch, M., Rosselló, J.M., Lechner, C., Lauterborn, W., Eisener, J., Mettin, R., 2021. Theory-assisted optical ray tracing to extract cavitation-bubble shapes from experiment. Exp. Fluids 62, 60. https://doi.org/10.1007/s00348-020-03075-6.

Lechner, C., Lauterborn, W., Koch, M., Mettin, R., 2020. Jet formation from bubbles near a solid boundary in a compressible liquid: numerical study of distance dependence. Phys. Rev. Fluids 5, 093604. https://doi.org/10.1103/PhysRevFluids.5.093604.

Lechner, C., Lauterborn, W., Koch, M., Mettin, R., 2019. Fast, thin jets from bubbles expanding and collapsing in extreme vicinity to a solid boundary: a numerical study. Phys. Rev. Fluids 4, 021601. https://doi.org/10.1103/PhysRevFluids.4.021601.

Mason, T.J., Cobley, A.J., Graves, J.E., Morgan, D., 2011. New evidence for the inverse dependence of mechanical and chemical effects on the frequency of ultrasound. Ultrason. Sonochem 18, 226–230. https://doi.org/10.1016/j.ultsonch.2010.05.008.

Mitsuzawa, S., Deguchi, S., Horikoshi, K., 2006. Cell structure degradation in Escherichia coli and Thermococcus sp. strain Tc-1-95 associated with thermal death resulting from brief heat treatment. FEMS. Microbiol. Lett 260, 100–105. https://doi.org/10.1111/j.1574-6968.2006.00301.x.

O'Connor, J., Akbar, F.B., Hutson, M.S., Page-McCaw, A., 2021. Zones of cellular damage around pulsed-laser wounds. PLoS. ONE 16, e0253032. https://doi.org/10.1371/journal.pone.0253032.

Ohl, C.-.D., Arora, M., Ikink, R., de Jong, N., Versluis, M., Delius, M., Lohse, D., 2006. Sonoporation from jetting cavitation bubbles. Biophys. J. 91, 4285–4295. https://doi.org/10.1529/biophysj.105.075366.

Paliwal, S., Mitragotri, S., 2006. Ultrasound-induced cavitation: applications in drug and gene delivery. Expert. Opin. Drug. Deliv 3, 713–726. https://doi.org/10.1517/17425247.3.6.713.

Pandur, Ž., Dular, M., Kostanjšek, R., Stopar, D., 2022. Bacterial cell wall material properties determine E. coli resistance to sonolysis. Ultrason. Sonochem. 83, 105919 https://doi.org/10.1016/j.ultsonch.2022.105919.

Patinglag, L., Melling, L.M., Whitehead, K.A., Sawtell, D., Iles, A., Shaw, K.J., 2021. Non-thermal plasma-based inactivation of bacteria in water using a microfluidic reactor. Water. Res. 201, 117321 https://doi.org/10.1016/j.watres.2021.117321.

Petkovšek, M., Hočevar, M., Dular, M., 2020. Visualization and measurements of shock waves in cavitating flow. Exp. Therm. Fluid. Sci 119, 110215. https://doi.org/10.1016/j.expthermflusci.2020.110215.

Potthoff, E., Ossola, D., Zambelli, T., Vorholt, J.A., 2015. Bacterial adhesion force quantification by fluidic force microscopy. Nanoscale 7, 4070–4079. https://doi.org/10.1039/C4NR06495J.

Prosperetti, A., 2004. Bubbles. Phys. Fluids 16, 1852–1865. https://doi.org/10.1063/1.1695308.

Quinto-Su, P.A., 2014. A microscopic steam engine implemented in an optical tweezer. Nat. Commun 5, 1–7. https://doi.org/10.1038/ncomms6889.

Rau, K.R., Quinto-Su, P.A., Hellman, A.N., Venugopalan, V., 2006. Pulsed laser microbeam-induced cell lysis: time-resolved imaging and analysis of hydrodynamic effects. Biophys. J 91, 317–329. https://doi.org/10.1529/biophysj.105.079921.

Reuter, F., Deiter, C., Ohl, C.-.D., 2022. Cavitation erosion by shockwave self-focusing of a single bubble. Ultrason. Sonochem 90, 106131. https://doi.org/10.1016/j.ultsonch.2022.106131.

Reuter, F., Ohl, C.-.D., 2021. Supersonic needle-jet generation with single cavitation bubbles. Appl. Phys. Lett 118, 134103. https://doi.org/10.1063/5.0045705.

Salmen, S.H., Alharbi, S.A., Faden, A.A., Wainwright, M., 2018. Evaluation of effect of high frequency electromagnetic field on growth and antibiotic sensitivity of bacteria. Saudi. J. Biol. Sci 25, 105–110. https://doi.org/10.1016/j.sjbs.2017.07.006.

Šarc, A., Oder, M., Dular, M., 2016. Can rapid pressure decrease induced by supercavitation efficiently eradicate Legionella pneumophila bacteria? Desalination. Water. Treat 57, 2184–2194. https://doi.org/10.1080/19443994.2014.979240.

Shamsborhan, H., Coutier-Delgosha, O., Caignaert, G., Abdel Nour, F., 2010. Experimental determination of the speed of sound in cavitating flows. Exp. Fluids 49, 1359–1373. https://doi.org/10.1007/s00348-010-0880-6.

Shiu, C., Zhang, Z., Thomas, C.R., 1999. A novel technique for the study of bacterial cell mechanical properties. Biotechnol. Techniq. 13, 707–713. https://doi.org/10.1023/A:1008919915047.

Simunič, U., Pipp, P., Dular, M., Stopar, D., 2020. The limitations of hydrodynamic removal of biofilms from the dead-ends in a model drinking water distribution system. Water. Res 178, 115838. https://doi.org/10.1016/j.watres.2020.115838.

Sinibaldi, G., Occhicone, A., Alves Pereira, F., Caprini, D., Marino, L., Michelotti, F., Casciola, C.M., 2019. Laser induced cavitation: plasma generation and breakdown shockwave. Phys. Fluids 31, 103302. https://doi.org/10.1063/1.5119794.

Sretenovic, S., Stojković, B., Dogsa, I., Kostanjšek, R., Poberaj, I., Stopar, D., 2017. An early mechanical coupling of planktonic bacteria in dilute suspensions. Nat. Commun 8, 213. https://doi.org/10.1038/s41467-017-00295-z.

Suslick, K.S., McNamara, W.B., Didenko, Y., 1999. Hot spot conditions during multi-bubble cavitation. Sonochemistry and Sonoluminescence. Springer, Netherlands, Dordrecht, pp. 191–204. https://doi.org/10.1007/978-94-015-9215-4_16.

Tinevez, J.-.Y., Perry, N., Schindelin, J., Hoopes, G.M., Reynolds, G.D., Laplantine, E., Bednarek, S.Y., Shorte, S.L., Eliceiri, K.W., 2017. TrackMate: an open and extensible platform for single-particle tracking. Methods 115, 80–90. https://doi.org/10.1016/j.ymeth.2016.09.016.

Tuson, H.H., Auer, G.K., Renner, L.D., Hasebe, M., Tropini, C., Salick, M., Crone, W.C., Gopinathan, A., Huang, K.C., Weibel, D.B., 2012. Measuring the stiffness of bacterial cells from growth rates in hydrogels of tunable elasticity. Mol. Microbiol 84, 874–891. https://doi.org/10.1111/j.1365-2958.2012.08063.x.

Vadillo-Rodríguez, V., Dutcher, J.R., 2011. Viscoelasticity of the bacterial cell envelope. Soft. Matter 7, 4101. https://doi.org/10.1039/c0sm01054e.

Valap Sealant, 2015. Cold spring harbor protocols 2015, pdb.rec082917. https://doi.org/10.1101/pdb.rec082917.

Verhaagen, B., Fernández Rivas, D., 2016. Measuring cavitation and its cleaning effect. Ultrason. Sonochem 29, 619–628. https://doi.org/10.1016/j.ultsonch.2015.03.009.

Vezenov, D., Barrett, M.J., 2013. Young's modulus of B. subtilis cell wall: measuring and modeling the elasticity of rod-like bacteria. Biophys. J. 104, 640a. https://doi.org/10.1016/j.bpj.2012.11.3537.

Wietzikoski Lovato, E.C., Gurgel Velasquez, P.A., dos Santos Oliveira, C., Baruffi, C., Anghinoni, T., Machado, R.C., Lívero, F.A.dos R., Sato, S.W., Martins, L.de A., 2018. High frequency equipment promotes antibacterial effects dependent on intensity and exposure time. Clin. Cosmet. Investig. Dermatol 11, 131–135. https://doi.org/10.2147/CCID.S156282. Volume.

Yusof, N.S.M., Babgi, B., Alghamdi, Y., Aksu, M., Madhavan, J., Ashokkumar, M., 2016. Physical and chemical effects of acoustic cavitation in selected ultrasonic cleaning applications. Ultrason. Sonochem 29, 568–576. https://doi.org/10.1016/j.ultsonch.2015.06.013.

Zeng, Q., Gonzalez-Avila, S.R., Dijkink, R., Koukouvinis, P., Gavaises, M., Ohl, C.-.D., 2018. Wall shear stress from jetting cavitation bubbles. J. Fluid. Mech 846, 341–355. https://doi.org/10.1017/jfm.2018.286.

Zevnik, J., Dular, M., 2022. Cavitation bubble interaction with compliant structures on a microscale: a contribution to the understanding of bacterial cell lysis by cavitation treatment. Ultrason. Sonochem 87, 106053. https://doi.org/10.1016/j.ultsonch.2022.106053.

Zevnik, J., Dular, M., 2021. Liposome destruction by a collapsing cavitation microbubble: a numerical study. Ultrason. Sonochem 78, 105706. https://doi.org/10.1016/j.ultsonch.2021.105706.

Zevnik, J., Dular, M., 2020. Cavitation bubble interaction with a rigid spherical particle on a microscale. Ultrason. Sonochem 69, 105252. https://doi.org/10.1016/j.ultsonch.2020.105252.

Zhou, Y., Yang, K., Cui, J., Ye, J.Y., Deng, C.X., 2012. Controlled permeation of cell membrane by single bubble acoustic cavitation. Journal. of. Controlled. Release 157, 103–111. https://doi.org/10.1016/j.jconrel.2011.09.068.

Zupanc, M., Kosjek, T., Petkovšek, M., Dular, M., Kompare, B., Širok, B., Stražar, M., Heath, E., 2014. Shear-induced hydrodynamic cavitation as a tool for pharmaceutical micropollutants removal from urban wastewater. Ultrason. Sonochem 21, 1213–1221. https://doi.org/10.1016/j.ultsonch.2013.10.025.

Zupanc, M., Pandur, Ž., Stepišnik Perdih, T., Stopar, D., Petkovšek, M., Dular, M., 2019. Effects of cavitation on different microorganisms: the current understanding of the mechanisms taking place behind the phenomenon. A review and proposals for further research. Ultrason. Sonochem 57, 147–165. https://doi.org/10.1016/j.ultsonch.2019.05.009.